Chemical Engineering Science 111 (2014) 364–380

Contents lists available at ScienceDirect

Chemical Engineering Science

journal homepage: www.elsevier.com/locate/ces

Viscoelastic fluid flow past a confined cylinder: Three-dimensional effects and stability

V.M. Ribeiro [a], P.M. Coelho [b], F.T. Pinho [b], M.A. Alves [a,*]

[a] Departamento de Engenharia Química, CEFT, Faculdade de Engenharia da Universidade do Porto, Rua Dr. Roberto Frias, 4200-465 Porto, Portugal
[b] Departamento de Engenharia Mecânica, CEFT, Faculdade de Engenharia da Universidade do Porto, Rua Dr. Roberto Frias, 4200-465 Porto, Portugal

HIGHLIGHTS

- Laminar flow of viscoelastic fluids past a confined circular cylinder.
- The 3D nature of the flow is assessed for a wide range of aspect ratios.
- Flow visualizations and PIV measurements are presented.
- The onset of flow instability is determined experimentally.

ARTICLE INFO

Article history:
Received 12 November 2013
Received in revised form
5 February 2014
Accepted 21 February 2014
Available online 4 March 2014

Keywords:
Viscoelastic flow
Rheology
Flow visualizations
Particle image velocimetry
Flow instabilities

ABSTRACT

The flow of viscoelastic fluids past a confined cylinder in a rectangular duct was investigated experimentally and numerically in order to assess the three-dimensional effects associated with cylinder aspect ratio (*AR*) and the fluid rheology. The blockage ratio was 50%, the cylinder aspect ratios were $AR=16$, 8 and 2, and the flow conditions tested varied from creeping flow conditions up to the onset of time-dependent flow. Three viscoelastic fluids were tested, namely a shear-thinning and two Boger fluids, and the results were compared against the numerical and experimental data for Newtonian fluids.

For the shear-thinning fluid, and in the range of Deborah numbers (*De*) studied ($0.025 < De < 0.99$), elastic instabilities appear upstream of the cylinder above a critical Deborah number, that depends on the aspect ratio. In contrast, for the Boger fluids the flow remained symmetric both upstream and downstream of the cylinder in the range of Deborah numbers studied ($De < 1.3$). For all non-Newtonian fluids studied, the streamwise velocity profiles show that the length required to achieve the fully developed velocity downstream of the cylinder increases with *De* and *AR*.

© 2014 Elsevier Ltd. All rights reserved.

1. Introduction

The flow past circular cylinders is of relevance for industrial applications and can be found in structural design and in the process industries. It is in the latter that typical applications involve fluids with non-Newtonian characteristics, as in heat exchangers, textile coating processes or in wastewater treatment, among others (Nishimura, 1986). In addition, the two-dimensional (2D) flow around a confined cylinder with 50% blockage ratio (*BR*, defined as the ratio between the cylinder diameter and the width of the channel) is a classical benchmark problem in computational rheology (Brown and McKinley, 1994).

There is a wealth of investigations on Newtonian fluid flow past an unconfined cylinder, which are summarized in the reviews of Telionis et al. (1992) and Williamson (1996) and in the books of Zdravkovich (1997, 2003). In contrast, much less is known about the interplay between the far flow field and the cylinder for fluids of complex nature such as the effects upon the flow around the cylinder and the vortex shedding phenomenon, of the aspect ratio (*AR*, defined as the ratio between the cylinder length and diameter), of the blockage ratio (*BR*) and also of the rheology of the working fluid.

The flow of Newtonian fluids past a cylinder in a rectangular channel is characterized by two geometrical ratios (e.g. *AR* and *BR*) and by the Reynolds number, which represents the relative importance of inertial forces relative to viscous forces. Sen et al. (2009) indicate the range $3.2 < Re_D < 7$ for the onset of downstream flow separation. The critical Reynolds number for the onset of laminar vortex shedding is found to be $Re_D \approx 47$ for high aspect ratios and increases when the aspect ratio decreases (Williamson, 1996;

* Corresponding author. Fax: +351 22508 1449.
E-mail addresses: vera.ribeiro@fe.up.pt (V.M. Ribeiro), pmc@fe.up.pt (P.M. Coelho), fpinho@fe.up.pt (F.T. Pinho), mmalves@fe.up.pt (M.A. Alves).

http://dx.doi.org/10.1016/j.ces.2014.02.033
0009-2509 © 2014 Elsevier Ltd. All rights reserved.

Sahin and Owens, 2004; Kumar and Mittal, 2006; Ribeiro et al., 2012). The work of Ribeiro et al. (2012) investigated the 3D effects on the laminar flow of a Newtonian fluid past a confined circular cylinder with $BR=50\%$ and showed good agreement between experimental results and numerical predictions. An unusual phenomenon was observed experimentally and confirmed numerically, consisting of intense velocity peaks downstream of the cylinder in the vicinity of the cylinder end walls, which are not reduced even when the aspect ratio of the cylinder increases. For the largest aspect ratios investigated ($AR=16$ and 8) the influence of the end walls on the local velocity peaks was predominant while for $AR<6$ the flow was found to be also influenced by the side walls, due to geometric confinement.

For viscoelastic fluids, the flow past a confined cylinder has also been thoroughly studied experimentally and numerically. Some of the experimental studies of non-Newtonian fluids around a confined cylinder refer only to steady creeping flow conditions (Manero and Mena, 1981; Shiang et al., 1997). Nevertheless, at higher flow rates (or Deborah numbers) when elastic instabilities occur, the flow becomes highly three-dimensional (3D), with steady complex structures developing upstream and downstream of the cylinder. At further higher flow rates, a second elastic instability develops and the flow becomes time-dependent (McKinley et al., 1993). McKinley (1991) investigated elastic instabilities in viscoelastic flow past a circular cylinder using a Boger fluid. The cylinder used in the experiments had a high aspect ratio ($AR=24$); thus the flow in the middle plane could be assumed as quasi-2D at low Deborah numbers. Above $De=1.30$, a cellular structure was observed in the spanwise direction; thus significant 3D effects were found even for such high AR geometry. Shiang et al. (2000) also investigated the flow past a confined cylinder ($AR=12$) with Boger fluids and observed the onset of steady three-dimensional flow, due to the formation of cellular structures in the wake of the cylinder, at a critical Deborah number between 0.14 and 0.21. The Boger fluid used by Shiang et al. (2000) was more viscous and elastic (thus, with a higher elasticity number) than the Boger fluid used by McKinley et al. (1993) and these differences can explain the discrepancy observed in the critical Deborah number. More recently, the experiments of Verhelst and Nieuwstadt (2004) showed the appearance of 3D effects near the walls in the flow past a confined cylinder in a rectangular duct with 50% blockage ratio and aspect ratio $AR=16$.

The onset of 3D effects in the viscoelastic fluid flow past a confined cylinder has also been reported in experimental studies using microfluidic devices (Li et al., 2010, 2012; Kenney et al., 2013). The downscaling of the channel dimensions in microfluidics amplifies the elastic effects, and simultaneously leads to a reduction of inertial effects. Recently, Kenney et al. (2013) investigated the fluid flow past a confined cylinder and identified two distinct elastic instabilities using dilute aqueous solutions of polyethylene oxide (PEO) for increasing flow rates. Initially a time-dependent downstream instability of disorderly streamlines was observed, followed by an upstream instability at higher flow rates, characterized by the occurrence of a detached upstream stagnation point and the formation of an upstream vortex.

Numerical investigations of non-Newtonian fluid flow past a cylinder are usually based on 2D calculations due to the expensive computational resources required for 3D simulations. For some viscoelastic fluids, such simulations showed the steady flow behind the cylinder to be characterized by the appearance of velocity overshoots, which depend significantly on the rheology of the fluid (Phan-Thien and Dou, 1999). Experimental and numerical studies of the viscoelastic flow past a gradual contraction, which can be qualitatively compared with the upstream flow around a cylinder, also show the appearance of velocity overshoots along the centreline and near the end walls upstream of the contraction for 3D geometries (Poole et al., 2007; Poole and Alves, 2009). These velocity overshoots near the walls, which were called the "cat's ears" phenomenon (Poole et al., 2007), are a manifestation of fluid elasticity and were qualitatively captured in the 3D numerical simulations of Poole and Alves (2009).

Despite the smaller number of works reporting 3D simulations, some studies analyzing the viscoelastic flow around a 3D cylinder have also appeared in the literature. Sahin and Wilson (2007) performed 2D and 3D viscoelastic fluid flow simulations around a confined circular cylinder in a channel with 50% blockage ratio, and analyzed the flow patterns up to a Weissenberg number (Wi) of 1.2. The converged 2D numerical results beyond $Wi=0.7$ indicate that the solutions are mesh dependent, at least in a small region in the wake of the cylinder, whereas for the 3D calculations the results at high Weissenberg numbers did not converge, due to the classical high Weissenberg number problem (HWNP) (Fattal and Kupferman, 2004). Sahin (2011) also simulated numerically the 2D and 3D flow of an Oldroyd-B fluid past a confined cylinder and concluded that at $Wi=0.7$ mesh convergence is still achieved in his calculations, even in the wake of the cylinder. However, no steady-state solution was possible for an Oldroyd-B fluid beyond $Wi=0.8$. Richter et al. (2010) studied numerically the 3D viscoelastic flow past a circular cylinder to assess the influence of viscoelasticity on the flow but their simulations were carried out at moderate Reynolds numbers ($100\leq Re\leq 300$). More recently, Tenchev et al. (2011) compared 2D and 3D flow simulations of an Oldroyd-B fluid around a confined cylinder and of a Rolie-Poly fluid flowing through a sudden contraction. In both cases, the results for 2D and 3D flows show significant differences, thus emphasizing the need for reliable 3D computations. More recently, Sahin (2013) investigated numerically the 3D creeping flow of an Oldroyd-B fluid past a confined cylinder in a rectangular channel and observed the appearance of a purely elastic instability in the wake of the cylinder, with the formation of cellular structures above a critical Weissenberg number between 1.2 and 1.6, in agreement with the experiments of McKinley et al. (1993).

The practical implementation of the flow of viscoelastic fluids past a confined cylinder is necessarily three-dimensional and it is clear from the previous works that their characteristics can be significantly different from those observed in a simplified two-dimensional geometry. Therefore, the primary goal of this work is the characterization of three-dimensional effects of the flow of viscoelastic fluids past a confined cylinder centered in a rectangular channel with 50% blockage ratio. This is achieved by considering the flows of two Boger fluids and one viscoelastic shear-thinning fluid in three different geometries having aspect ratios of $AR=16$, 8 and 2. The flows analyzed varied from creeping flow conditions (low Reynolds number) up to the onset of elastic induced time-dependent flow, which corresponds to the range of Reynolds numbers between $0.008<Re<3.2$ and Deborah numbers between $0.025<De<0.99$. This work was preceded by a similar investigation involving the laminar flow of Newtonian fluids at low Reynolds numbers (Ribeiro et al., 2012). Numerical predictions were also carried out in order to predict the Newtonian and non-Newtonian fluid flows. These numerical predictions, together with the results of Ribeiro et al. (2012), will be used here to assess and separate the effects of elasticity from those of shear-thinning viscosity.

The remainder of this paper is organized as follows: the experimental set-up and techniques are described in Section 2, while Section 3 presents the rheological characterization of the fluids used. The governing equations and a brief outline of the numerical method are described in Section 4. Section 5 presents and discusses the experimental results and compares them with the corresponding Newtonian fluid flow. In Section 6 the main conclusions are summarized.

2. Experiments

2.1. Experimental set-up

The measurements were carried out in the test section schematically represented in Fig. 1, which is made of transparent acrylic. The whole closed loop rig, described in detail in Ribeiro et al. (2012) (cf. Fig. 1), is here only briefly outlined. The 1700 mm-long test section has a rectangular cross-section with a width (H) of 20 mm and a variable depth (h) in order to assess the effect of the aspect ratio ($AR=h/D$) of the geometry. This is achieved by moving one of the end walls (parallel to the xy plane), allowing the depth (h) of the cross-section to be 160 mm, 80 mm or 20 mm (accuracy ± 100 μm), resulting in $AR=16$, 8 or 2, respectively. The 10 mm-diameter cylinder is located 630 mm downstream of the duct inlet and is positioned at the mid-plane to define a symmetric geometry with a 50% blockage ratio ($BR=D/H$). The origin of the coordinate system represented in Fig. 1 is located at the center of the cylinder.

2.2. Experimental techniques

The experiments included flow visualization using long-time exposure streak photography and detailed velocity measurements using particle image velocimetry (PIV). A detailed description of the operating principles of both techniques can be found in Ribeiro et al. (2012).

Both techniques were used at the various xy planes marked in Fig. 2 to assess the spanwise variation of the flow field. The planes under study for each AR are at the same absolute distance of the end wall, but most experiments focus on the centreplane, $z/R=0$.

The tracer particles used were hollow glass spheres with 10 μm diameter (HGS-10, Dantec Dynamics) at a weight concentration of 30 ppm for the flow visualizations and for the measurements with PIV, the particle concentration was chosen in order to follow the recommendations for PIV of having at least 5–10 particles per interrogation area (Adrian, 2005).

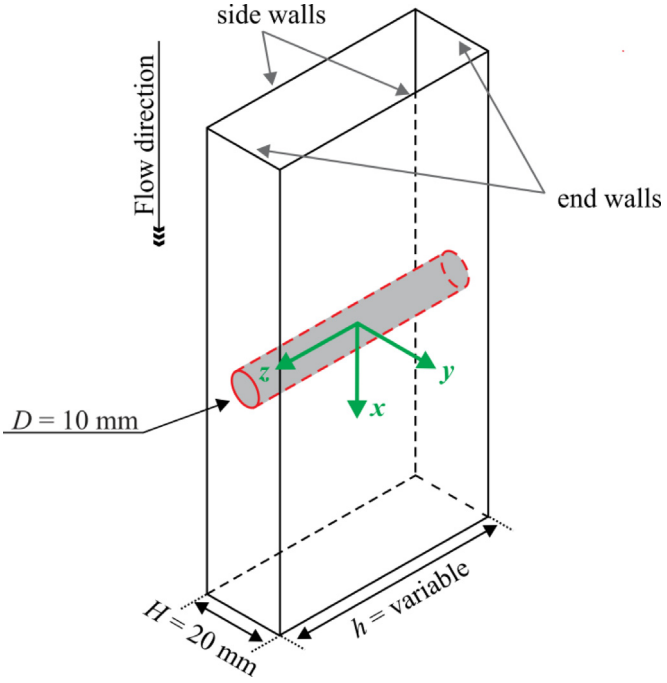

Fig. 1. Test section and coordinate system.

In the visualization of flow patterns using long-time exposure streak photography the exposure time was adjusted according to the flow rate and varied between 1 s and 30 s.

In the measurements of the velocity fields with the PIV system, the time between two consecutive pulses varied between 1 ms and 2 s, depending on the flow rate, the plane of measurement and the aspect ratio under study. For all flow rates, at least 50 pairs of images were acquired and the velocity field was determined by processing the images with FlowManager v4.60 software (Dantec Dynamics), using an adaptive-correlation algorithm.

3. Fluid characterization

The fluids used were a shear-thinning viscoelastic fluid and two Boger fluids, all prepared with different concentrations of polyacrylamide (PAA). In addition, flow data for a Newtonian fluid (Ribeiro et al., 2012) is also used for comparison purposes. The shear-thinning fluid was an aqueous solution of PAA at a weight concentration of 1000 ppm and the Boger fluids were aqueous solutions of glycerin (85% w/w) with PAA at weight concentrations of 200 ppm and 400 ppm, with 1% NaCl. All fluids were seeded with tracer particles, as described in Section 2. In order to minimize bacteriological growth in the fluids and minimize their inherent degradation, a biocide was added at a concentration of 25 ppm (kathon LXE, Rohm and Haas). The density (ρ) of the fluids was measured at 293.2 K using a pycnometer. The composition and the density of the fluids are presented in Table 1.

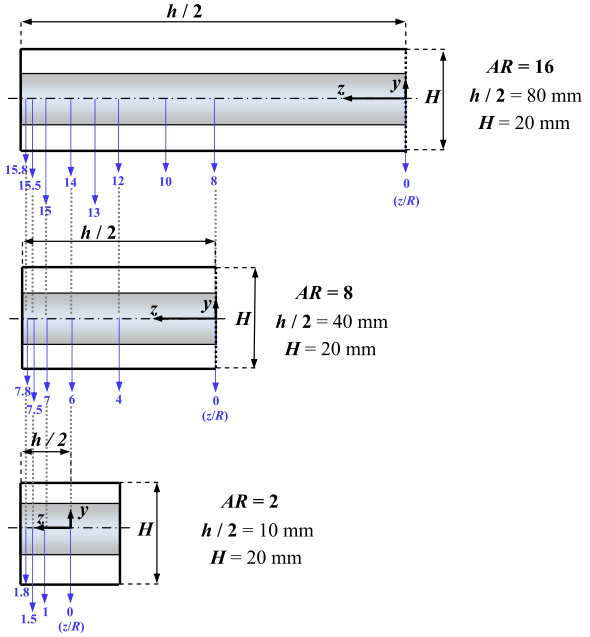

Fig. 2. Planes under study for $AR=16$, 8 and 2 along the cylinder at different values of $|z/R|$. Adapted from Ribeiro et al. (2012).

Table 1
Fluid composition (mass concentration) and density measured at 293.2 K.

Fluid	PAA (ppm)	Glycerin (%)	Water (%)	NaCl (%)	Kathon (ppm)	ρ (kg/m^3)
Newtonian	–	–	100	–	25	999.8
Shear-thinning – PAA1000	1000	–	99.90	–	25	1001.5
Boger – PAA200	200	85.05	13.91	1.02	25	1225.8
Boger – PAA400	400	85.06	13.89	1.01	25	1226.3

The rheological characterization of the fluids was carried out in shear and extensional flow. The shear measurements were made using two rotational rheometers: Physica MCR 301 (Anton Paar) with a 75 mm cone-plate system with 1° angle; AR-G2 (TA Instruments) with a 40 mm cone-plate system with 2° angle (Boger fluids only). The data are represented as hollow and filled symbols for the Physica MCR 301 and for the AR-G2 rheometers, respectively.

In the steady shear measurements for the viscoelastic shear-thinning fluid (PAA1000), the flow curve was measured at different temperatures (283.5–303.2 K) and the time–temperature superposition principle was used in order to obtain the master curve at the reference temperature (T_0=293.2 K). The corresponding shift factor is defined as (Dealy and Plazek, 2009)

$$a_T = \frac{\eta(T)}{\eta(T_0)}\frac{T_0}{T}\frac{\rho_0}{\rho}, \tag{1}$$

where $\eta(T_0)$ is the shear viscosity at the reference temperature T_0, $\eta(T)$ is the shear viscosity at a given temperature T, ρ_0 is the density at the reference temperature T_0 and ρ is the density at temperature T. Since the temperature variation for the rheological measurements is small, the fluid density does not change significantly and the shift factor simplifies to (Dealy and Plazek, 2009)

$$a_T = \frac{\eta(T)}{\eta(T_0)}. \tag{2}$$

Fig. 3 shows the steady-state shear viscosity master curve, together with the corresponding fit to a generalized Newtonian fluid (GNF) model. The Carreau model (Carreau, 1972) was used for the viscosity function, which is defined as

$$\eta = \eta_s + \frac{\eta_0 - \eta_s}{[1+(\Lambda\dot{\gamma})^2]^{(1-n)/2}}. \tag{3}$$

The parameters of this fitted model were η_0=2.0 Pa s; η_s=0.004 Pa s, Λ=25 s, and n=0.38.

In the steady shear measurements for the Boger fluids (PAA200 and PAA400) the flow curve was measured at different temperatures (288.2–298.2 K). As for the shear-thinning fluid, the time–temperature superposition principle was used in order to obtain the master curve at the reference temperature (T_0=293.2 K). Fig. 4a shows nearly constant viscosities of 0.152 Pa s and 0.174 Pa s for the PAA200 and PAA400 fluids, respectively, in the shear rate range of $1 < \dot{\gamma}/s^{-1} < 1000$. The shear viscosities of these diluted polymer solutions are similar since these are essentially

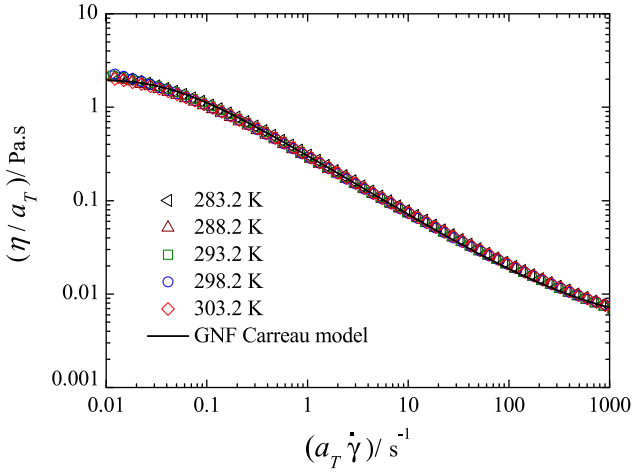

Fig. 3. Steady shear viscosity of the shear-thinning fluid (PAA1000). The symbols represent the experimental data measured at different temperatures and the solid line the fit by a Carreau model.

determined by the viscous solvent. Fig. 4b shows the dynamic shear viscosity (η') and G'/ω^2 as a function of ω. Note that as $\omega \to 0$, η' tends to the steady shear viscosity when $\dot{\gamma} \to 0$ as it should, despite the different rheometer used. A two-mode plus solvent model was used to fit G' and η' and the details of the linear viscoelastic spectra determined at T_0=293.2 K are shown in Table 2.

The fitted two-mode model (solid lines) overlaps the rheological measurements shown in Fig. 4b and it is clear that, within the measured frequency range, a two-mode Oldroyd-B model is adequate to represent the linear viscoelastic behaviour of the Boger fluids. The solvent viscosity, η_s=0.126 Pa s, corresponds to the dynamic viscosity of the Newtonian solvent used in the preparation of the fluids. Using the parameters of the two-mode model presented in Table 2, an average relaxation time can be calculated as

$$\lambda = \frac{1}{\eta_p}\sum_{k=1}^{2}\eta_k\lambda_k, \tag{4}$$

where $\eta_p = \sum_{k \neq solvent}\eta_k$, leading to λ=130 ms for the Boger fluid PAA200 and λ=197 ms for the Boger fluid PAA400.

The extensional behaviour of the solution was measured at the reference temperature (T_0=293.2 K) using a capillary break-up extensional rheometer (Haake CaBER 1, Thermo Scientific). The characteristic relaxation time in extensional flow was determined by fitting the experimental data of $\log[D(t)]$ vs. time in the region of elasto-capillary balance which obeys the following equation (Entov and Hinch, 1997):

$$\frac{D}{D_0} = e^{(-t/3\lambda)}, \tag{5}$$

where D_0 is the diameter of the filament at the reference time t=0 and D is the diameter at the time t. The measurements were performed using two circular plates with a diameter of 6 mm. As shown in Fig. 5 the experimental data were fitted and the relaxation times obtained were λ=104 ms for the shear-thinning fluid PAA1000 (cf. Fig. 5a), λ=86.7 ms for the PAA200 Boger fluid and λ=97.7 ms for the PAA400 Boger fluid (cf. Fig. 5b).

The two methods used to determine λ lead to slightly different values, as expected. However, since the values obtained are of the same order of magnitude, this gives some reliability to the results obtained with the Boger fluids. The relaxation time determined in extensional flow is thought to be more appropriate for the flow under study, since the flow around the cylinder is strongly dominated by the extensional stresses on the wake of the cylinder. Therefore, in the remaining of this paper, the relaxation time determined using the CABER device will be used. We note, however, that the relaxation time obtained for the semi-diluted shear-thinning fluid is much smaller than the value that can be estimated from the flow curve (Fig. 3). The onset of shear-thinning usually occurs at a shear rate which is approximately the inverse of the relaxation time. From Fig. 3 we can estimate a relaxation time in shear of the order of 20 s, which is more than two orders of magnitude higher than the relaxation time determined in the CaBER device and also a bit too high. For the shear-thinning fluid the true relaxation time is likely to lie between these two values so that the relaxation time used in the remaining calculations of this study should be viewed as a rough estimate, and the *De* values calculated are most probably too small.

4. Governing equations and numerical method

The experimental results were simulated using an implicit finite-volume method with a time marching pressure-correction algorithm (Oliveira et al., 1998). The governing equations

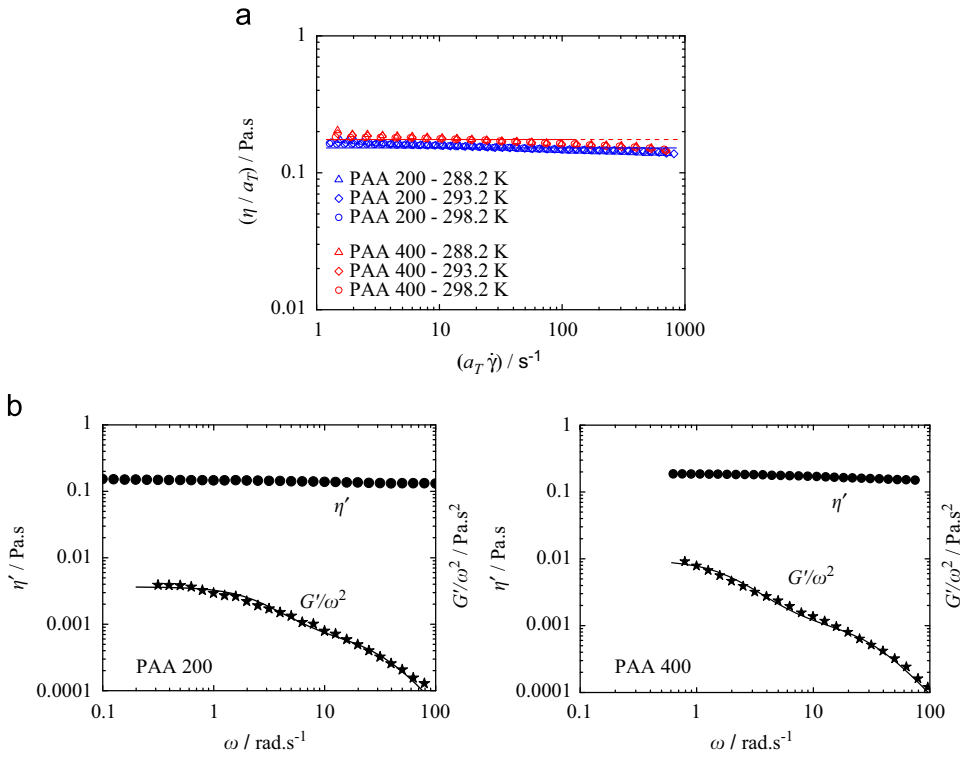

Fig. 4. Material functions of Boger fluids PAA200 and PAA400 in (a) steady shear flow (the symbols represent the experimental data measured at different temperatures); (b) small amplitude oscillatory shear flow. The solid lines represent the fits by the two-mode Oldroyd-B model.

Table 2
Linear viscoelastic spectra for the Boger fluids.

Mode k	**PAA 200**		**PAA 400**	
	λ_k (s)	η_k (Pa s)	λ_k (s)	η_k (Pa s)
1	0.030	0.020	0.031	0.031
2	0.38	0.008	0.50	0.017
Solvent	–	0.126	–	0.126

describing the isothermal laminar flow of an incompressible fluid are the mass conservation

$$\nabla \cdot \mathbf{u} = 0, \tag{6}$$

and the momentum equation

$$\rho\left(\frac{\partial \mathbf{u}}{\partial t} + \nabla \cdot \mathbf{uu}\right) = -\nabla p + \nabla \cdot \boldsymbol{\tau}, \tag{7}$$

where $\mathbf{u}$ represents the velocity vector, ρ the fluid density, t the time, p the pressure and $\boldsymbol{\tau}$ the extra-stress tensor, which is given as a sum of a Newtonian solvent with a polymeric contribution ($\boldsymbol{\tau} = \boldsymbol{\tau}_\mathbf{s} + \boldsymbol{\tau}_\mathbf{p}$). For Newtonian fluids, the polymeric contribution is null, $\boldsymbol{\tau}_\mathbf{p} = \mathbf{0}$, and the Newtonian solvent component $\boldsymbol{\tau}_\mathbf{s}$ is defined as

$$\boldsymbol{\tau}_\mathbf{s} = \eta_s(\nabla \mathbf{u} + \nabla \mathbf{u}^{\mathrm{T}}) = 2\eta_s \mathbf{D}, \tag{8}$$

where η_s is the constant solvent viscosity and $\mathbf{D}$ is the deformation rate tensor.

For the numerical calculations of the shear-thinning viscoelastic fluid, a generalized Newtonian fluid (GNF) was used based on the Carreau viscosity model. The numerical calculations with this GNF model do not describe accurately the flow in the vicinity of the cylinder, where elastic effects are more relevant, but are able to predict with good accuracy the flow far from the cylinder under fully developed flow conditions, where the shear viscosity is more relevant.

In the numerical predictions using the Carreau model the polymeric contribution to the extra-stress tensor is neglected, $\boldsymbol{\tau}_\mathbf{p} = \mathbf{0}$, and the shear-thinning viscosity function is introduced via the $\boldsymbol{\tau}_\mathbf{s}$ term

$$\boldsymbol{\tau}_\mathbf{s} = 2\eta(\dot{\gamma})\mathbf{D}, \tag{9}$$

with the function $\eta(\dot{\gamma})$ given by the Carreau model (Eq. (3)).

For the numerical calculations of the Boger fluid flow, the polymeric contribution is included and the fluid is described using the Oldroyd-B model, given by

$$\boldsymbol{\tau}_\mathbf{p} + \lambda\left(\frac{\partial \boldsymbol{\tau}_\mathbf{p}}{\partial t} + \nabla \cdot \mathbf{u}\boldsymbol{\tau}_\mathbf{p}\right) = \eta_P(\nabla \mathbf{u} + \nabla \mathbf{u}^T) + \lambda(\boldsymbol{\tau}_\mathbf{p} \cdot \nabla \mathbf{u} + \nabla \mathbf{u}^T \cdot \boldsymbol{\tau}_\mathbf{p}) \tag{10}$$

where η_P is the shear viscosity of the polymer. The fitted parameters of the Carreau and the Oldroyd-B models were described in Section 3.

The numerical method is based on a time-marching version of the SIMPLEC pressure correction algorithm formulated for collocated variables (Oliveira et al., 1998). The discretization of the governing equations is based on central differences for diffusive terms and on the CUBISTA high-resolution scheme (Alves et al., 2003) for the convective terms both in the momentum and in constitutive equations. The computational domain was mapped using non-orthogonal block-structured meshes. Extensive sets of calculations were carried out by Ferreira (2006) to estimate the numerical uncertainty and select an adequate mesh to provide mesh independent results. To generate the mesh the flow domain was divided into 24 blocks and within each block the cells were concentrated near the cylinder region and channel walls, as illustrated in Fig. 6, for $AR = 8$.

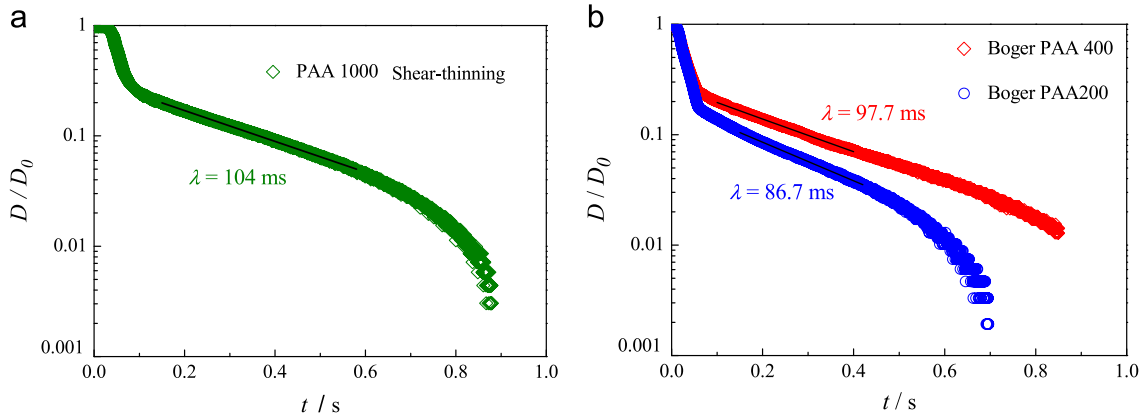

Fig. 5. Diameter of the filament measured as a function of time using the CaBER device for (a) shear-thinning fluid PAA1000; (b) Boger fluids PAA200 and PAA400.

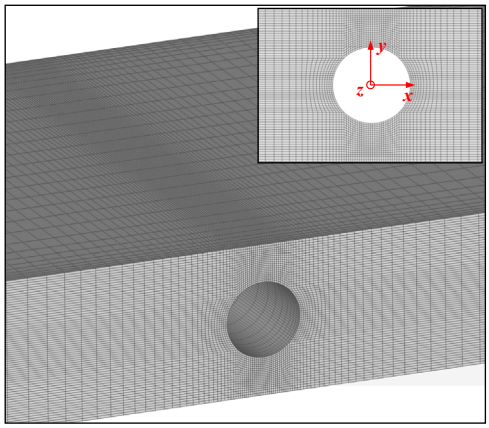

Fig. 6. Zoomed view of the mesh used in the numerical simulations for $AR=8$.

5. Results and discussion

The viscoelastic fluid flow around a confined cylinder was characterized using flow visualizations and detailed velocity field measurements using PIV. The experiments were carried out at an average temperature of 293 K, and ranged between 291.7 K and 294.7 K. The experimental work was conducted with the three viscoelastic fluids previously described: shear-thinning PAA1000, Boger PAA200 and Boger PAA400. The experiments were carried out for $AR=16$, 8 and 2 using the shear-thinning fluid, whereas for the Boger fluids the experiments were restricted to the $AR=16$ geometry. The selection of the Boger fluids, i.e., constant viscosity elastic fluids, allows the isolation of viscoelastic effects, without the added complexity of shear-thinning effects.

A thorough experimental and numerical investigation of Newtonian fluid flow around a confined cylinder for $AR=16$, 8 and 2 was presented in Ribeiro et al. (2012). Some of the previous results are used in this work to provide a reference scenario to compare with the viscoelastic fluid flow.

The flow characteristics of Newtonian fluids depend on two geometrical ratios (AR and BR) and on the Reynolds number (Re), here defined as

$$Re=\frac{\rho UR}{\eta}, \tag{11}$$

where U is the bulk upstream velocity ($U=Q/Hh$), R is the radius of the cylinder and η is the shear viscosity of the fluid. For the shear-thinning fluid the viscosity in Eq. (11) is evaluated at the characteristic shear rate $\dot{\gamma}=U/R$.

The flow of viscoelastic fluids is also characterized using the Deborah number (De), which represents the ratio of a characteristic time of the fluid (λ) and a characteristic flow time scale (R/U):

$$De=\frac{\lambda U}{R}. \tag{12}$$

The Deborah numbers calculated were based on the relaxation time of the fluid measured in the CaBER, as previously discussed.

5.1. Shear-thinning fluid – PAA1000

5.1.1. Flow patterns

The effect of De on the flow patterns at the symmetry plane ($z/R=0$) is illustrated in some representative photographs shown in Figs. 7, 8 and 9 for $AR=16$, 8 and 2, respectively, obtained using long-time exposure streak photography. The vertical and horizontal lines inside the cylinder are a guide to the eye to highlight possible flow asymmetry. For all AR at low De, symmetric flow patterns are observed upstream and downstream of the cylinder (cf. Figs. 7a, 8a and 9a). Beyond a critical Deborah number, De_c, which depends on AR, an elastic instability occurs upstream of the cylinder, near the forward stagnation point, as seen in Figs. 7b–d, 8b–d, and 9b. At these critical flow conditions, we observe the onset of steady upstream asymmetric flow instability, which is particularly noticeable on the right side of the images. For $AR=16$ and 8, the instability appears at $De_c\approx 0.04$, whereas $De_c\approx 0.4$ for $AR=2$, suggesting that the end walls have a stabilizing effect. Note that the inherent uncertainties of the experimental technique based on the visual inspection of the flow pathlines only provide an estimate value of De_c. In all cases the flow asymmetry magnitude increases with De. Far upstream of the cylinder, the flow is symmetric, which highlights the influence of the cylinder on the onset of elastic instability. Then, as De is increased further, the steady asymmetry intensifies and the flow eventually becomes time-dependent. Again, we remark that the relaxation time used in the calculation of De for the shear-thinning fluid is probably too small; therefore it comes as no surprise that the values of De_c for the shear-thinning fluid are so small.

In order to illustrate the extension of the elastic instability along the spanwise direction, Fig. 10 shows the projected pathlines at different z-planes along the cylinder axis for $De=0.31$, $Re=0.47$ and $AR=8$, which corresponds to a flow condition under the steady asymmetric regime. In the middle plane ($z/R=0$), the flow is distorted towards one side of the cylinder in the cross-stream direction (here to the right side), but as we approach the end wall ($z/R\rightarrow 8$), the flow asymmetry progressively spans to both sides of

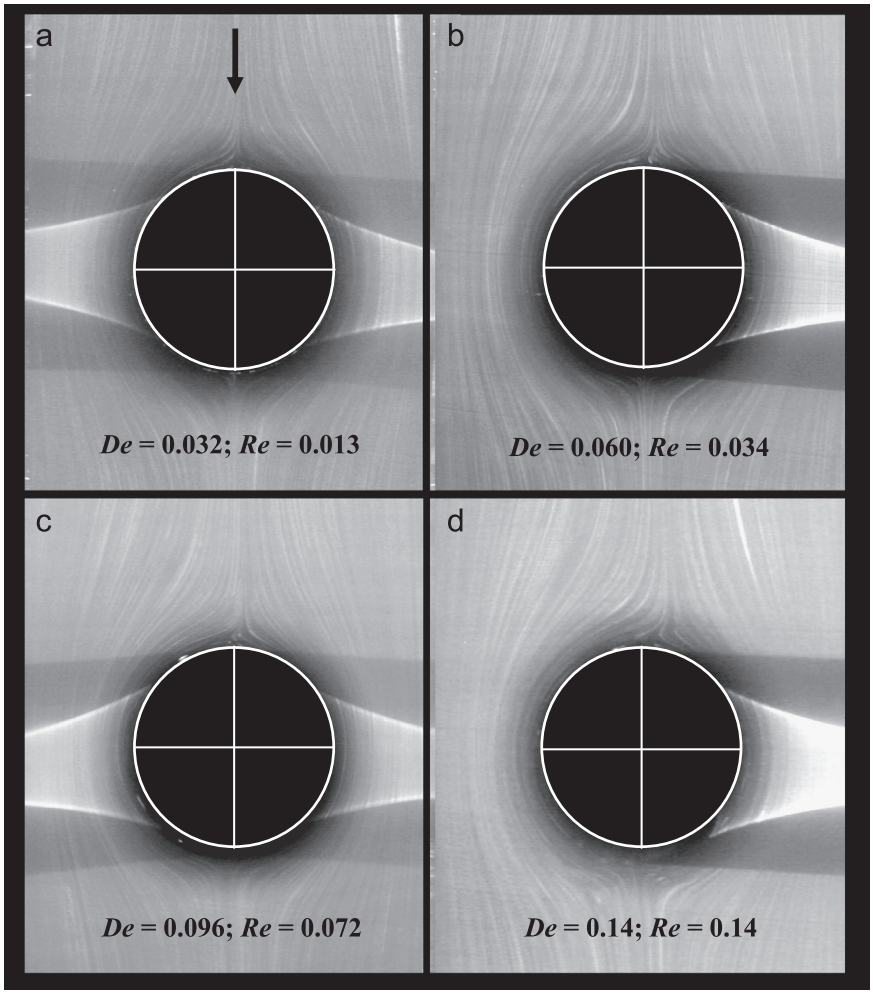

Fig. 7. Long-time exposure streak photography: effect of elasticity on the flow patterns at the symmetry plane ($z/R=0$) for $AR=16$, using the PAA1000 shear-thinning fluid.

the cylinder. The same pattern also occurs for $AR=16$ and 2, but the corresponding plots are not shown for conciseness.

Fig. 11 shows the influence of AR on the extent of the elastic instability at constant De. For $De\approx 0.14$ and $Re=0.14$, the elastic instability is clearly noticeable for $AR=16$ (and similarly for $AR=8$ – not shown), but for $AR=2$ the flow is still symmetric. Therefore, for the same flow conditions the elastic instability is intensified as AR increases, although for large AR there is no significant influence, as demonstrated by the similar De_c values for $AR=16$ and 8.

When the flow rate is increased further, leading to higher Deborah numbers, but still at relatively low Reynolds numbers ($Re<1$) the flow asymmetry intensifies until the flow eventually becomes time-dependent, with a periodic behaviour. Fig. 12 shows a sequence of *instantaneous* pathlines visualized for $AR=8$ at $De=0.39$ and $Re=0.72$, where we can clearly observe the flow unsteadiness. The same phenomenon is also observed for $AR=16$ and $AR=2$ at high De. We note that for small values of Re, as those reported in this section, the Newtonian flow was shown previously to be perfectly symmetric and steady (Ribeiro et al., 2012), and thus the steady asymmetric flow and the unsteady flow at higher De reported here are due to the elasticity of the fluid.

5.1.2. Velocity field

Fig. 13 shows the influence of AR upon profiles of the streamwise dimensionless velocity component, u/U, measured along the centreline ($y/R=0$ and $z/R=0$) for the shear-thinning fluid at various De. We also compare these results with the corresponding numerically computed velocity profiles for a Newtonian fluid under creeping flow conditions and a Carreau Generalized Newtonian fluid, to highlight the influences of viscoelasticity and shear-thinning effects. The numerical results obtained with the GNF model at the same Re are not able to predict accurately the velocity profile near the cylinder, where elastic effects are dominant, but are able to predict adequately the fully developed velocity far from the cylinder, where the shear flow and viscous shear stresses are dominant.

Far from the cylinder, the measured velocity profiles are fully developed and the shear-thinning behaviour of the viscoelastic fluid is clear from the lower centreline velocities (plug like behaviour), when compared to the Newtonian velocity profiles. The numerical predictions obtained with the GNF model confirm that the upstream and downstream lengths of the rectangular duct are sufficient to achieve the fully developed velocity profile with the shear-thinning flow. The experimental results show that as the flow approaches the cylinder, the velocity decreases up to the forward stagnation point and this effect is spatially more far reaching at higher AR and De. Comparing the experimental results with the GNF predictions for the fully developed velocity, for the two highest AR ($AR=16$ and 8) the deceleration starts upstream of $x/R=-15$ (not shown) whereas for $AR=2$ the deceleration starts at $x/R\approx -8$ (cf. Fig. 13). The development lengths required for the downstream flow redevelopment increase with De, for all AR under study, in agreement with the results obtained by McKinley

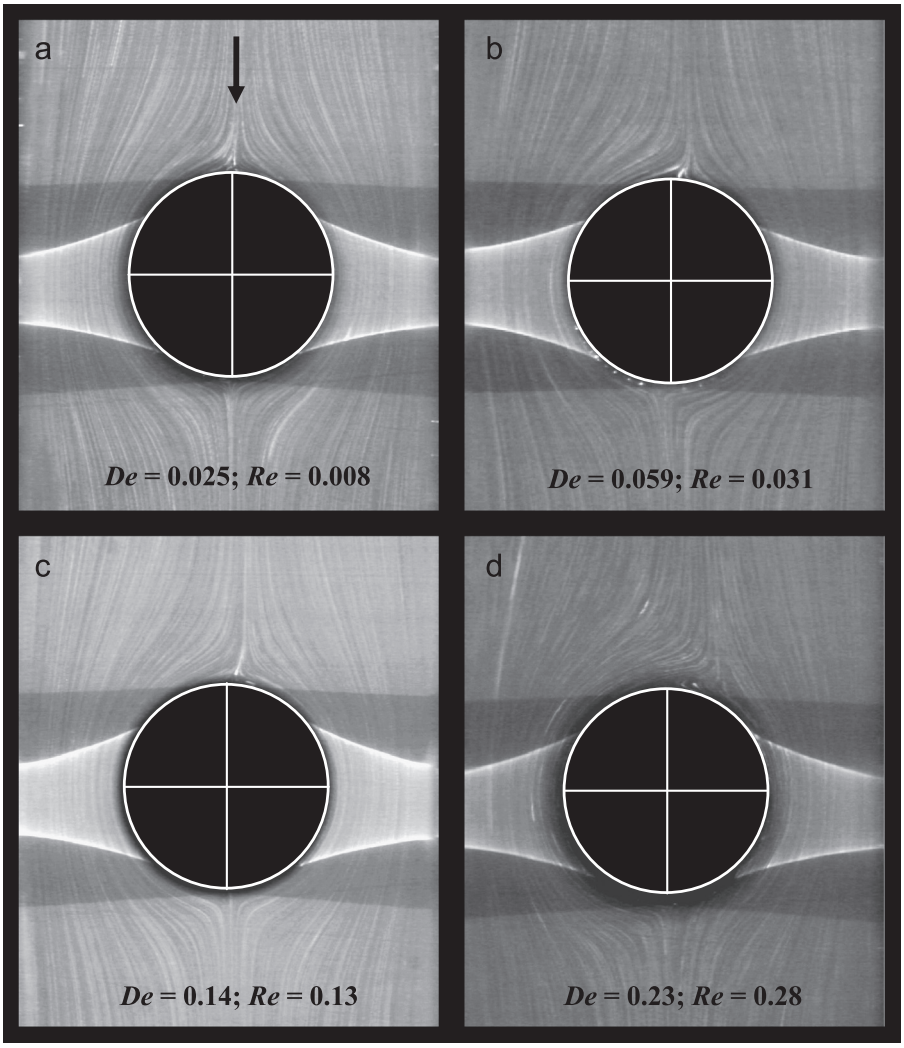

Fig. 8. Long-time exposure streak photography: effect of elasticity on the flow patterns at the symmetry plane ($z/R=0$) for $AR=8$, using the PAA1000 shear-thinning fluid.

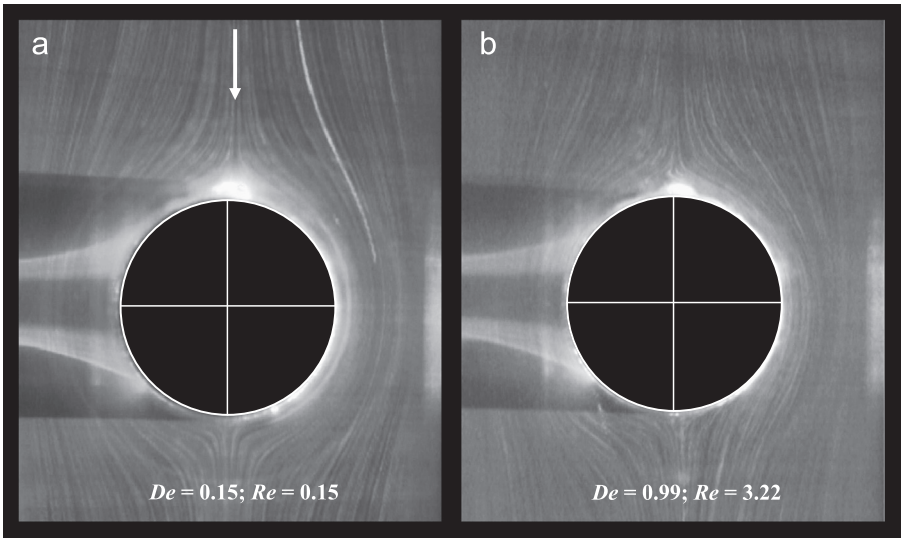

Fig. 9. Long-time exposure streak photography: effect of elasticity on the flow patterns at the symmetry plane ($z/R=0$) for $AR=2$, using the PAA1000 shear-thinning fluid.

et al. (1993). For similar values of *De*, for example $De \approx 0.26$–0.3 and for $AR=16$ and 8 the flow redevelopment only occurs at $x/R > 15$, while for $AR=2$ the velocity redevelopment occurs at $x/R \approx 10$ (cf. Fig. 13). Thus, the length required for velocity recovery downstream of the cylinder is influenced by *De*, increasing progressively as viscoelasticity increases, and is also influenced

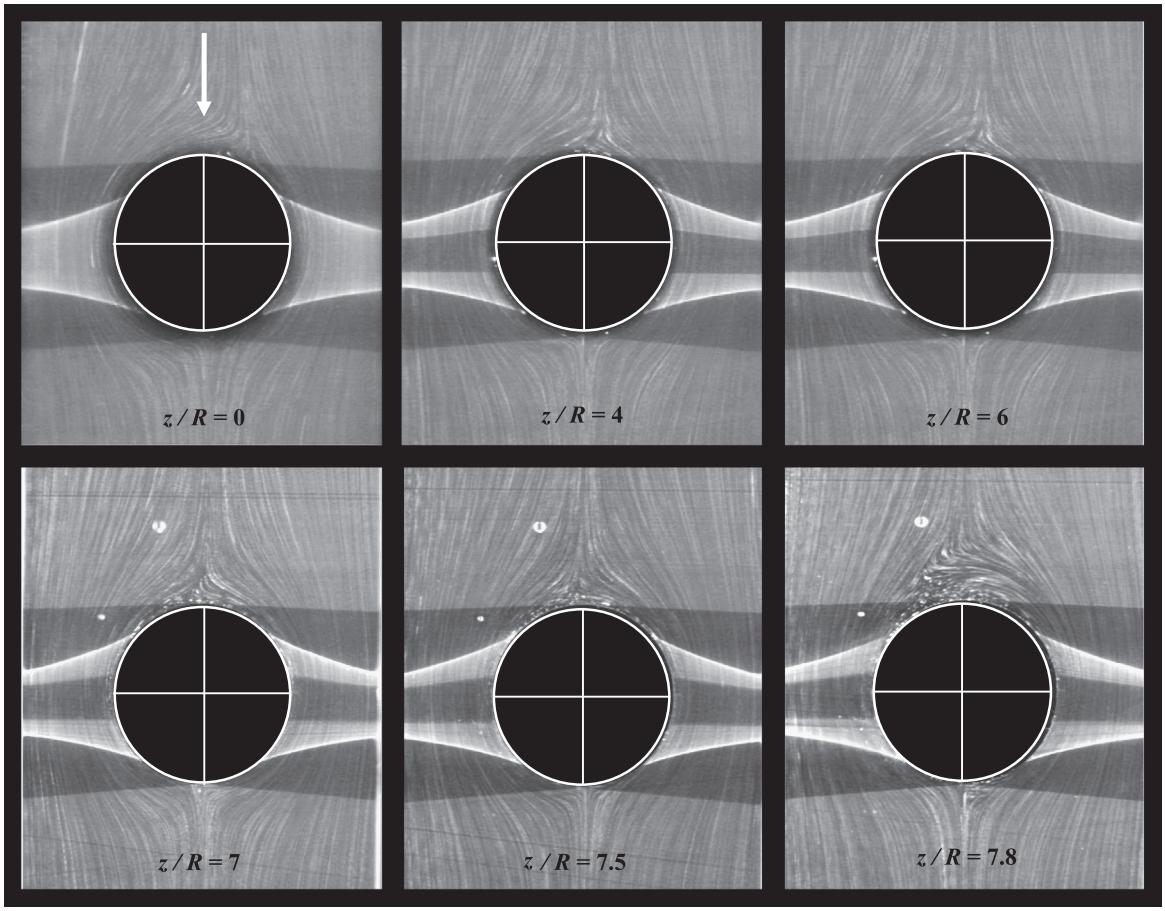

Fig. 10. Long-time exposure streak photography: flow patterns obtained with the PAA1000 shear-thinning fluid at different planes along the z-direction for $De=0.31$, $Re=0.47$ and $AR=8$.

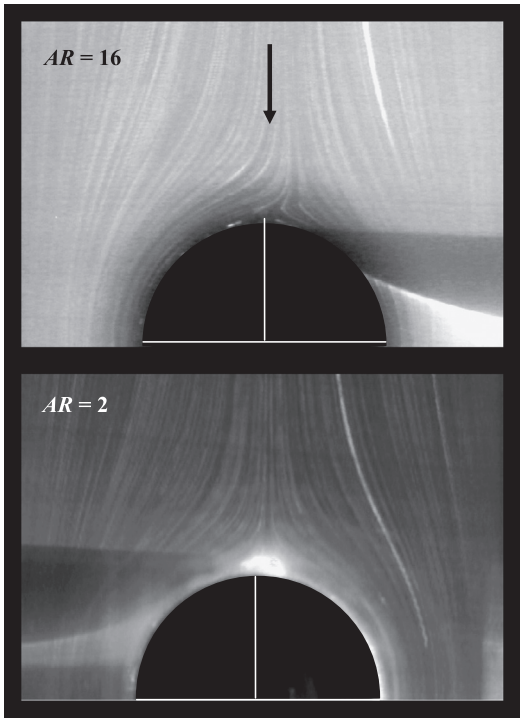

Fig. 11. Long-time exposure streak photography: flow patterns obtained at the symmetry plane ($z/R=0$) as a function of AR using the PAA1000 shear-thinning fluid at $De \approx 0.14$ and $Re \approx 0.14$.

by AR, decreasing as the degree of confinement increases, which suggests that the end walls have a stabilizing effect, as already observed in the flow visualizations.

As AR decreases up to $AR=2$, the fully developed centreline velocity increases, due to geometric confinement. A similar effect also occurs with Newtonian fluids, with the maximum fully developed dimensionless velocity occurring for a square channel ($AR=2$), for which a dimensionless velocity $u/U=2.096$ is obtained (cf. Fig. 13c), in agreement with the analytical solution for Newtonian fluid flow in a rectangular channel (White, 1991).

The velocity profiles measured near the end walls, along the line at $z/R=(AR-1)$ and $y/R=0$, are presented in Fig. 14. The chosen plane, $z/R=(AR-1)$, corresponds to the location of a local maximum velocity for Newtonian fluids (Ribeiro et al., 2012). Fig. 14 also includes numerical predictions for the corresponding Newtonian fluid under creeping flow conditions ($Re \to 0$) and numerical predictions obtained with the GNF model at the same Re as in the experiments.

For the higher AR investigated ($AR=16$ and 8) and upstream of the cylinder, in this near end-wall region the flow accelerates until there is a maximum velocity, which is reached between $-5 \leq x/R \leq -3$, followed by a significant reduction of the velocity, due to the approaching cylinder. The acceleration starts well upstream of the cylinder, at $x/R \approx -15$. A similar effect also occurs for Newtonian fluids under creeping flow conditions as shown by the full lines corresponding to the numerical predictions. Downstream of the cylinder there is also a velocity overshoot, before the fully developed velocity profile is asymptotically approached at $x/R > 15$ (for Newtonian creeping flow there is flow symmetry upstream

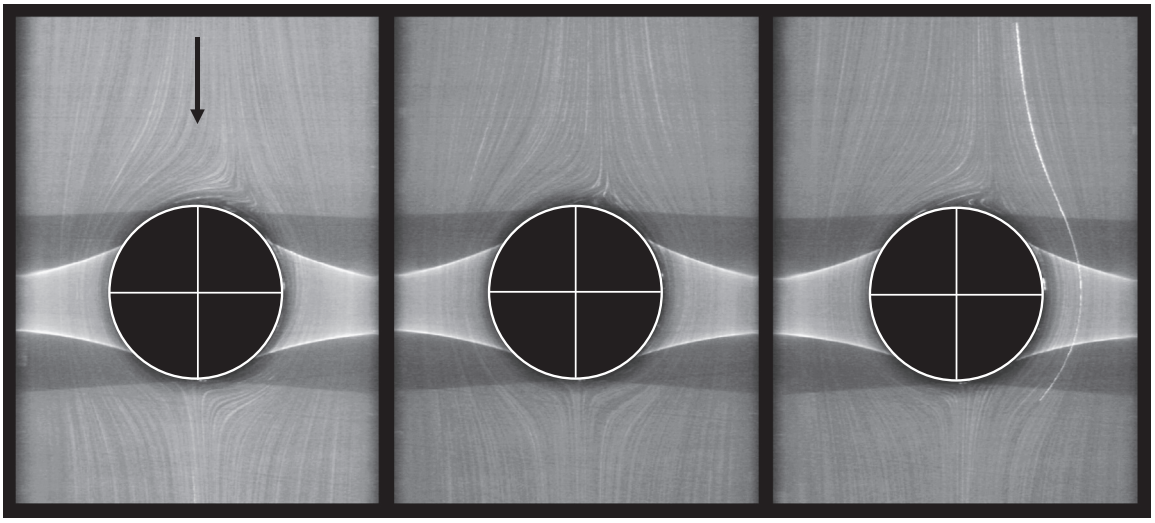

Fig. 12. Long-time exposure streak photography showing the flow patterns obtained with the PAA1000 shear-thinning fluid for $AR=8$, $De=0.39$ and $Re=0.72$, at the symmetry plane ($z/R=0$) and at three different instants along the flow oscillation cycle.

and downstream of the cylinder, due to the flow reversibility). In contrast, for $AR=2$ the velocity decreases (upstream of the cylinder) and increases (downstream of the cylinder) monotonically until the fully developed velocity is approached. As for the centreplane $z/R=0$, and in contrast to what happens for $AR=16$ and $AR=8$, the deceleration upstream of the cylinder starts closer to the cylinder at $x/R\approx -8$ and the downstream fully developed velocity is already achieved at $x/R\approx 10$.

The differences between the experimentally measured and numerically computed velocity profiles for the GNF model show that for $AR=16$ and 8 the increasing magnitude of the velocity peaks with De is due to the elasticity of the fluid, since the GNF model is purely viscous. For $AR=2$, the elasticity of the fluid leads to an increase of the required length to achieve the fully developed velocity.

Comparing the velocity profiles near the end walls with those at the centreplane, and for all AR, the fully developed velocity decreases as expected. It is important at this stage to remind the reader that the higher De cases plotted in Figs. 13 and 14 are asymmetric close and upstream of the cylinder ($De>De_c$).

Fig. 15 shows the spanwise evolution of the measured profiles of the streamwise velocity at several values of z/R (cf. Fig. 2) taken on the $y/R=0$ centreplane for all AR and at $De\approx 0.12$, corresponding to symmetric flow for $AR=2$ and asymmetric flow for $AR=16$ and $AR=8$. As for the Newtonian fluids, the fully developed velocity is higher on the centreline and decreases as the flow approaches the end walls for all AR.

For $AR=16$ and 8, in the profiles closer to the centreplane (up to $z/R=12$ for $AR=16$ and up to $z/R=4$ for $AR=8$) the velocity profiles are similar to that at $z/R=0$, except for a slight decrease of the fully developed velocity. Near the end walls ($z/R\geq 13$ for $AR=16$ and $z/R\geq 6$ for $AR=8$), both upstream and downstream of the cylinder, a velocity peak is observed at $x/R\approx -4$ and $x/R\approx 4$. The exact locations of the velocity maxima upstream and downstream of the cylinder depend on De. The changes observed in the velocity profiles behaviour closer to the end walls are related to the influence created by the presence of those walls, which is similar to that seen for Newtonian fluids (Ribeiro et al., 2012). However, for viscoelastic fluids it is enhanced by fluid elasticity, which is also responsible for flow asymmetry absent from the corresponding Newtonian creeping flow case. For $AR=2$ the velocity profiles upstream and downstream of the cylinder are monotonic (no near wall maximum velocity peaks), in agreement with the observations at the centreplane.

Figs. 16 and 17 show transverse profiles of the normalized streamwise velocity at two upstream ($x/R=-6$ and -2) and two downstream locations ($x/R=2$ and 6) at the symmetry plane ($z/R=0$), for $De\approx 0.03$ and 0.3. These figures pertain to $AR=8$ and 2, respectively, thus representing the high and low AR cases (the results for $AR=16$ and $AR=8$ are similar). The lines represent the numerical predictions for the corresponding Newtonian fluid under creeping flow conditions ($Re\to 0$). It is important to remind the reader that the flow for the higher De ($De\approx 0.3$) and $AR=8$ in Fig. 16 is asymmetric, since $De>De_c$. However these asymmetries are not visible in Fig. 16 because the upstream profile closer to the cylinder is at $x/R=-2$ and at this distance the local steady instability is still not strong enough to influence significantly the velocity profiles, and hence only half profiles are shown.

For $AR=8$ and far upstream of the cylinder, at $x/R=-6$, the flow is slightly influenced by the presence of the cylinder (Fig. 16a), due to the flow deceleration already reported in Fig. 13 with regard to the symmetry plane ($y/R=0$). At this same location ($x/R=-6$) and for $AR=2$ (Fig. 17a) the influence of the cylinder is nearly negligible, as shown previously in Fig. 13c. At $x/R=-6$ the velocities are always higher on the symmetry plane than near the side walls. For $AR=8$ the effect of the approaching cylinder occurs earlier with the increase of De. This also happens for $AR=2$, but still closer to the cylinder, i.e., at $|x/R|<6$. Thus the effect of the cylinder is shown again to occur earlier as AR increases.

Closer to the cylinder, e.g. at $x/R=-2$ (Figs. 16b and 17b), the flow is now significantly influenced by the presence of the cylinder for all AR investigated and the velocities are higher at $y/R\approx 1$–1.5 than at the symmetry plane as the former corresponds to the gap between the cylinder and the side walls. As can be observed in Figs. 16b and 17b for $De\approx 0.3$ the velocity peaks occur at $|y/R|\approx 1.5$ while for $De\approx 0.03$ the velocity peaks occur at $|y/R|\approx 1.3$, regardless of AR. Thus, at $x/R=-2$ the location of the velocity peaks depends on De, and is found to be closer to the side walls as well as more pronounced when De increases.

Figs. 16c,d and 17c,d show that the redevelopment of the velocity profile downstream of the cylinder occurs further downstream for the higher De, in agreement with the profiles showed earlier in Fig. 13b and c for the streamwise velocity along the centreline. Downstream of the cylinder, at $x/R=2$, the flow is still influenced by the bluff body for $AR=8$, regardless of De, and the streamwise velocities are higher near the side walls than at the symmetry plane. At this location, the velocity peak occurs at

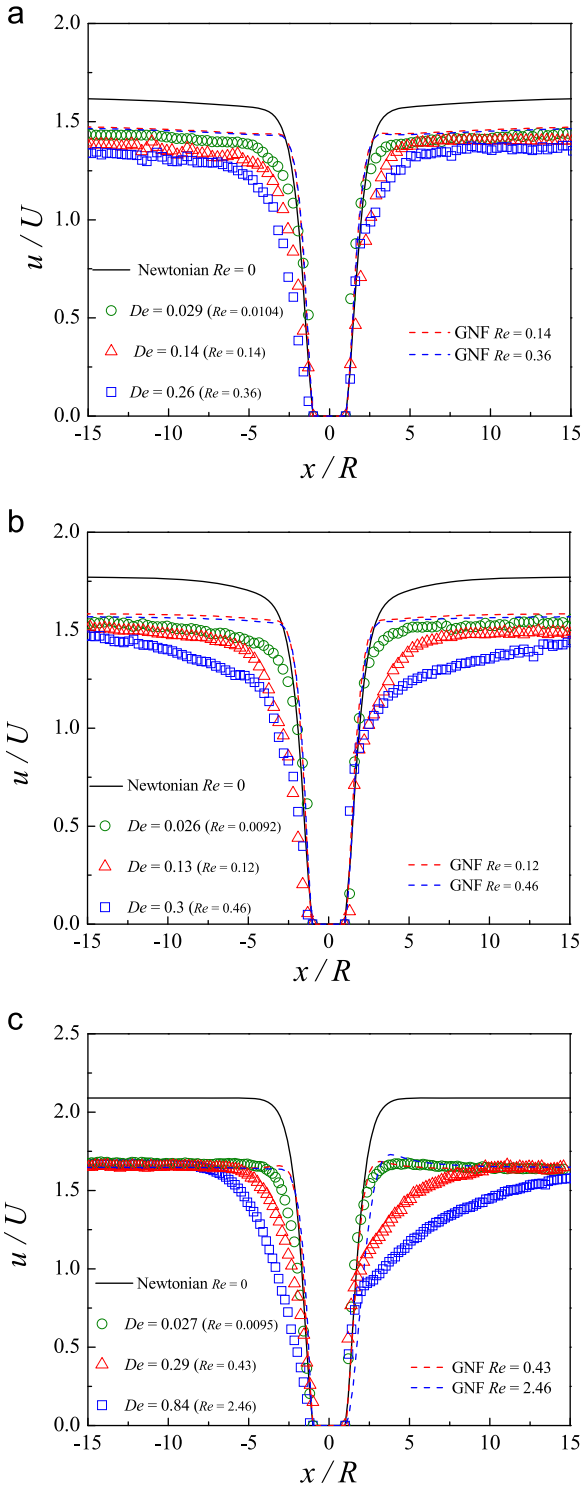

Fig. 13. Streamwise velocity profiles along the centreline ($z/R=0$, $y/R=0$) for the shear-thinning fluid as a function of *De* (symbols) and comparison with numerical predictions with the GNF model (dashed lines) and inertia-less Newtonian flow: (a) $AR=16$, (b) $AR=8$, and (c) $AR=2$.

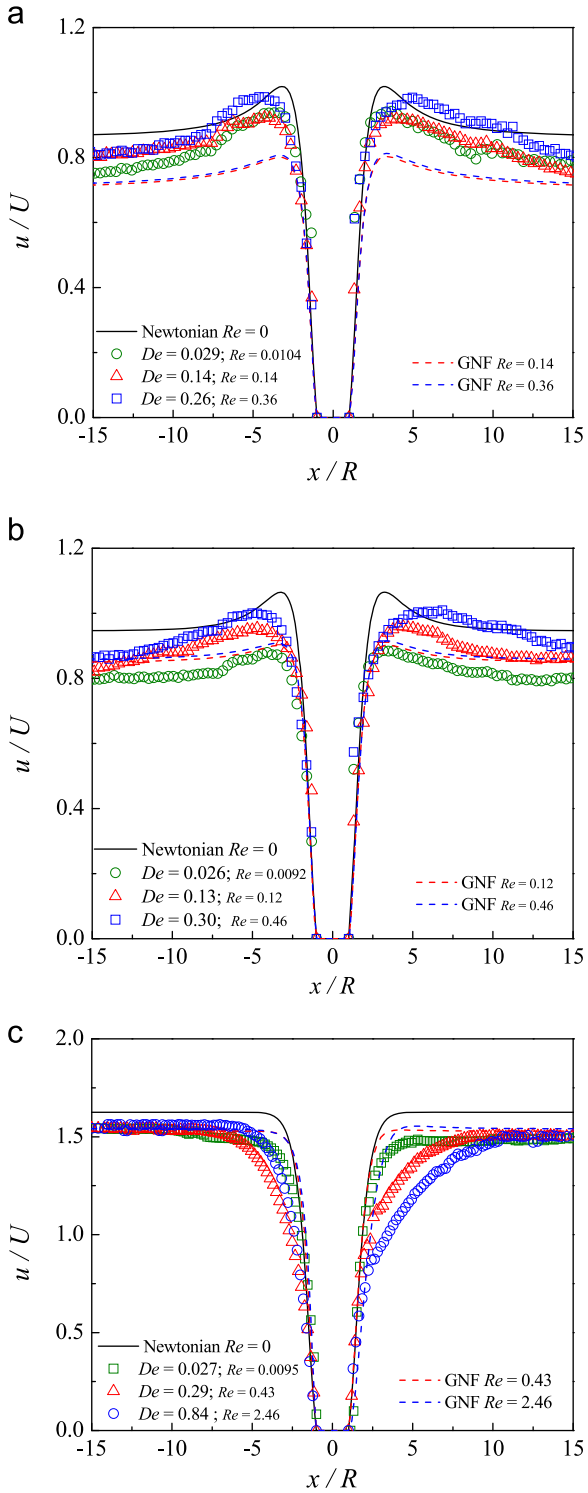

Fig. 14. Streamwise velocity profiles along the line $z/R=AR-1$ and $y/R=0$ for the shear-thinning fluid as a function of *De* (symbols). Comparison with numerical predictions with the GNF model (dashed lines) and inertia-less Newtonian flow: (a) $AR=16$, (b) $AR=8$, and (c) $AR=2$.

$|y/R| \approx 1.2$, regardless of *De*. For $AR=2$ the velocity is higher on the symmetry plane for lower *De*, (cf. Fig. 17c for $De=0.027$), but when *De* increases further the velocities become higher near the side walls. Thus, at this streamwise location ($x/R=2$) and at lower *De*, the effect of the duct confinement overlaps the effect of the presence of the cylinder. Moving downstream to $x/R=6$ (Figs. 16d and 17d) the flow is still dependent on *De*, and the velocity field is still developing, in agreement with the observations of Fig. 13.

5.2. Boger fluids

5.2.1. Flow patterns

Fig. 18 shows the effect of *De* on the flow patterns observed for the Boger fluids at the central plane ($z/R=0$) for $AR=16$ (PAA200 in Fig. 18a and PAA400 in Fig. 18b). The range of *De* studied with these fluids ($0.01 < De < 0.14$) is below that for the shear-thinning fluids and so the flow remains symmetric upstream

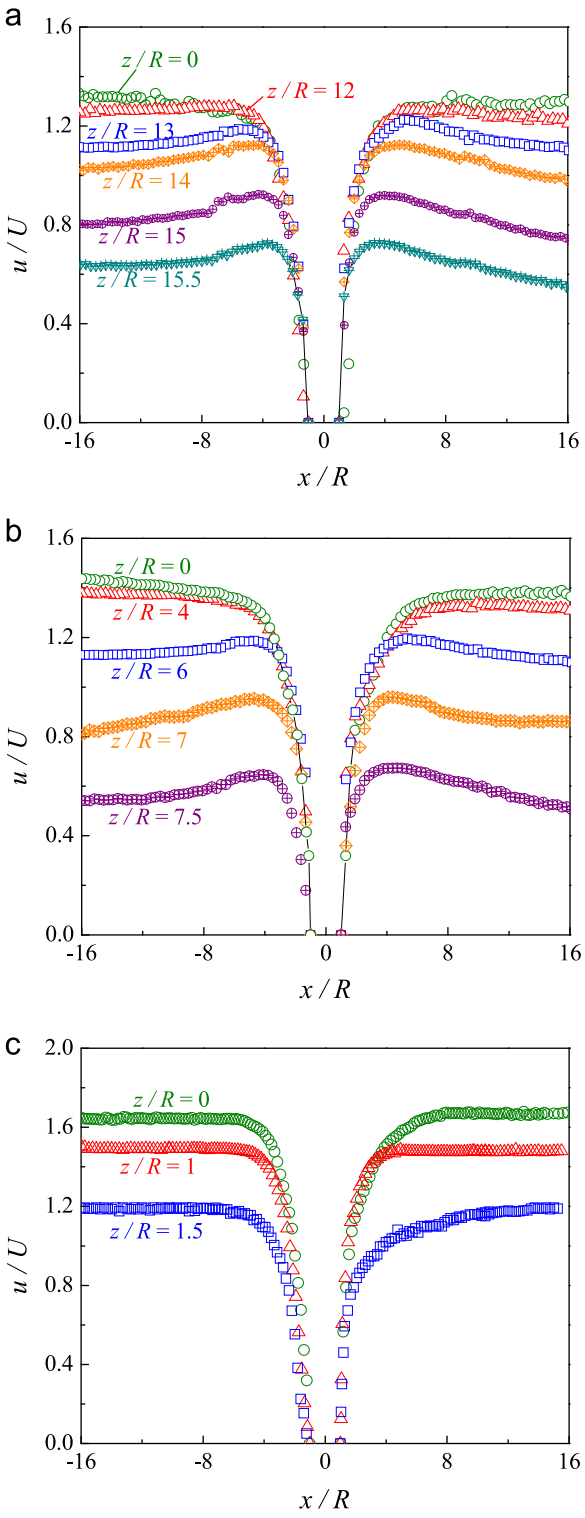

Fig. 15. Streamwise profiles of the streamwise velocity component at the symmetry plane ($y=0$) at different values of z/R along the cylinder axis for the shear-thinning fluid at $De=0.12$ and $Re=0.10$: (a) $AR=16$, (b) $AR=8$, and (c) $AR=2$.

and downstream of the cylinder. Fig. 18 includes the corresponding streamlines predicted numerically using the Oldroyd-B model, which agrees with the experimental data. The higher viscosities of the Boger fluids reduce the maximum flow rates achievable in the rig, thus limiting the values of *De* that can be studied.

Symmetric flow upstream and downstream of the cylinder was also observed in the spanwise direction, as shown in Fig. 19 for PAA200 Boger fluid at $De=0.13$, including the corresponding streamlines predicted numerically using the Oldroyd-B model, which are in agreement with the experiments.

The comparison with the experimental data shows good agreement, and it is found that in this range of flow conditions the influence of fluid elasticity is not significant in qualitative terms. However, at higher flow rates the elastic effects are enhanced and the onset of elastic-driven flow instabilities is expected to occur, as observed in the experiments of McKinley et al. (1993) and Shiang et al. (2000), and in the large-scale parallel simulations of Sahin (2013).

5.2.2. Velocity field

Fig. 20 shows the streamwise dimensionless velocity profiles along the centreline ($y/R=0$, $z/R=0$) for $AR=16$, using both PAA200 and PAA400 Boger fluids. The symbols represent the experimental data and lines represent the corresponding numerical predictions obtained with the Oldroyd-B model. Careful inspection shows that the experimental velocity profiles for both Boger fluids are similar and they only start to differ by a small amount downstream of the cylinder at the higher *De* achieved numerically (also plotted in Fig. 20), and for that reason the results presented below only refer to the Boger fluid PAA200. The small differences observed between the results of Boger fluids PAA200 and PAA400 are primarily due to the difference between their viscosity ratios (β, ratio of the solvent to total viscosities) and similarly for the two fitted Oldroyd-B models used in the simulations. The good agreement between the experimental results and the numerical predictions for $De \approx 0.13$ validates the numerical calculations for $AR=16$. Consequently, to further explore the influences of *AR* and elasticity, numerical computations using the Oldroyd-B model were carried out for the $AR=8$ and 2 cases, as discussed next.

Fig. 21 shows the influence of *AR* upon the dimensionless streamwise velocity along the centreline ($y/R=0$, $z/R=0$) for the PAA200 Boger fluid and as a function of *De*. Fig. 21a includes the experimental results (symbols) and numerical predictions obtained with the Oldroyd-B model fitted to the PAA200 Boger fluid (full lines) for $AR=16$, whereas Fig. 21b and c only shows the numerical predictions for $AR=8$ and $AR=2$, respectively. Fig. 21 also includes the numerical computations for Newtonian fluid flows (dashed lines) at the same flow conditions as for the PAA200 Boger fluid, i.e., with the same density, shear viscosity and for the same mean velocity (i.e. same *Re*) in order to isolate the influence of elasticity on the velocity field.

For all *AR*, the fully developed dimensionless velocity profile upstream of the cylinder is independent of flow rate (or *De*) since the fluid has a constant shear viscosity and the shape of such velocity profile is exclusively determined by the shear stress profile (the second normal stress difference is negligible). However, the flow upstream is influenced by the presence of the cylinder, due to the necessary flow deceleration up to the forward stagnation point, and this effect depends on *AR*. The deceleration starts at $x/R \approx 13$ for $AR=16$ and 8, while for $AR=2$ it starts at $x/R \approx 5$. Downstream of the cylinder, the required length to achieve the fully developed velocity (the corresponding value is indicated as dash–dot lines) increases with *De* and also depends on the *AR*. The fully developed velocity is achieved at $x/R > 15$ for $AR=16$ and 8 and earlier at $x/R \approx 12$ for $AR=2$, because of geometric confinement. Note that the fully developed dimensionless velocity on the centreline is the same for all these constant shear viscosity fluids and agree with the analytical solutions for Newtonian fluids in rectangular ducts, as shown previously by Ribeiro et al. (2012).

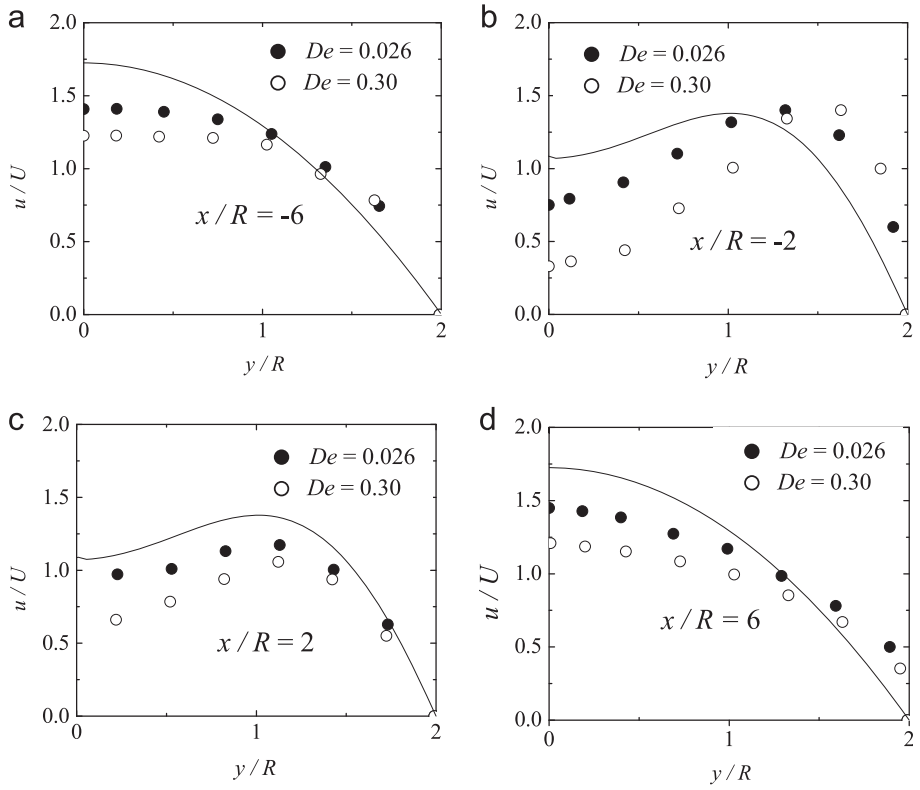

Fig. 16. Streamwise variation of the transverse profiles of the streamwise velocity component at the $z/R=0$ symmetry plane for the flow of the PAA1000 shear-thinning fluid at $AR=8$ for $De=0.026$, $Re=0.009$ and $De=0.30$, $Re=0.46$: (a) $x/R=-6$; (b) $x/R=-2$; (c) $x/R=2$; (d) $x/R=6$. The lines represent the numerical predictions for the corresponding Newtonian fluid under creeping flow conditions ($Re\rightarrow 0$).

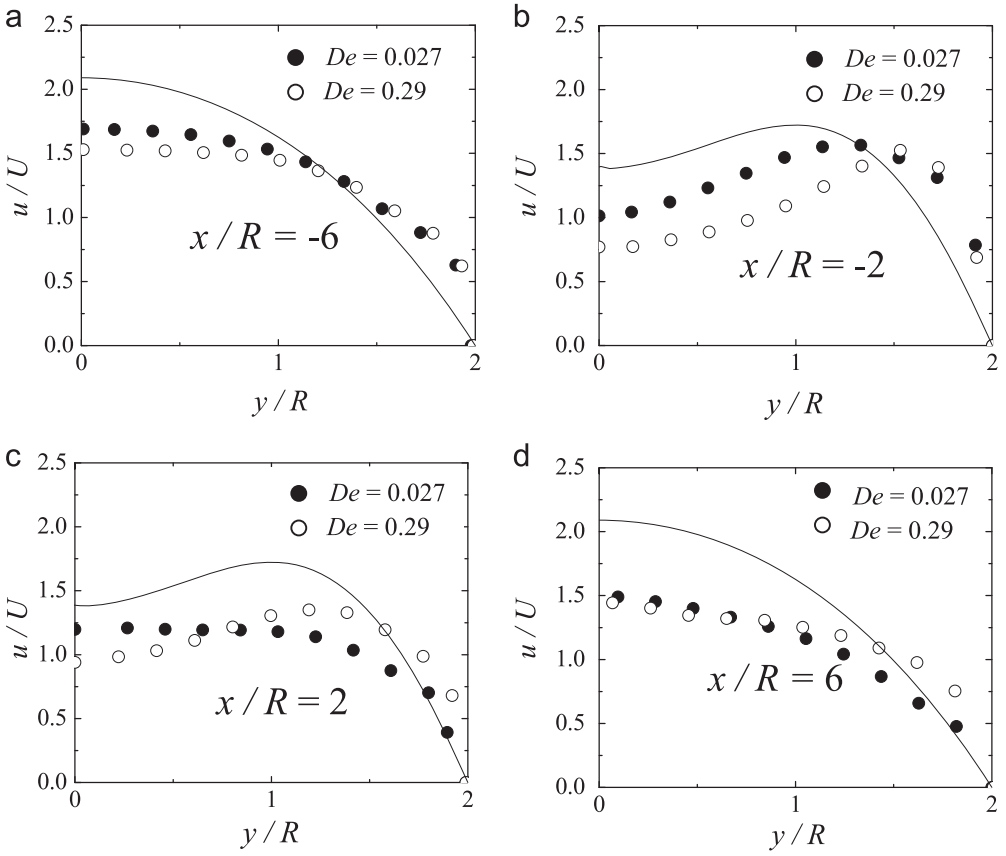

Fig. 17. Streamwise variation of the transverse profiles of the streamwise velocity component at the $z/R=0$ symmetry plane for the flow of the PAA1000 shear-thinning fluid at $AR=2$ for $De=0.027$, $Re=0.0095$ and $De=0.29$, $Re=0.43$: (a) $x/R=-6$; (b) $x/R=-2$; (c) $x/R=2$; (d) $x/R=6$. The lines represent the numerical predictions for the corresponding Newtonian fluid under creeping flow conditions ($Re\rightarrow 0$).

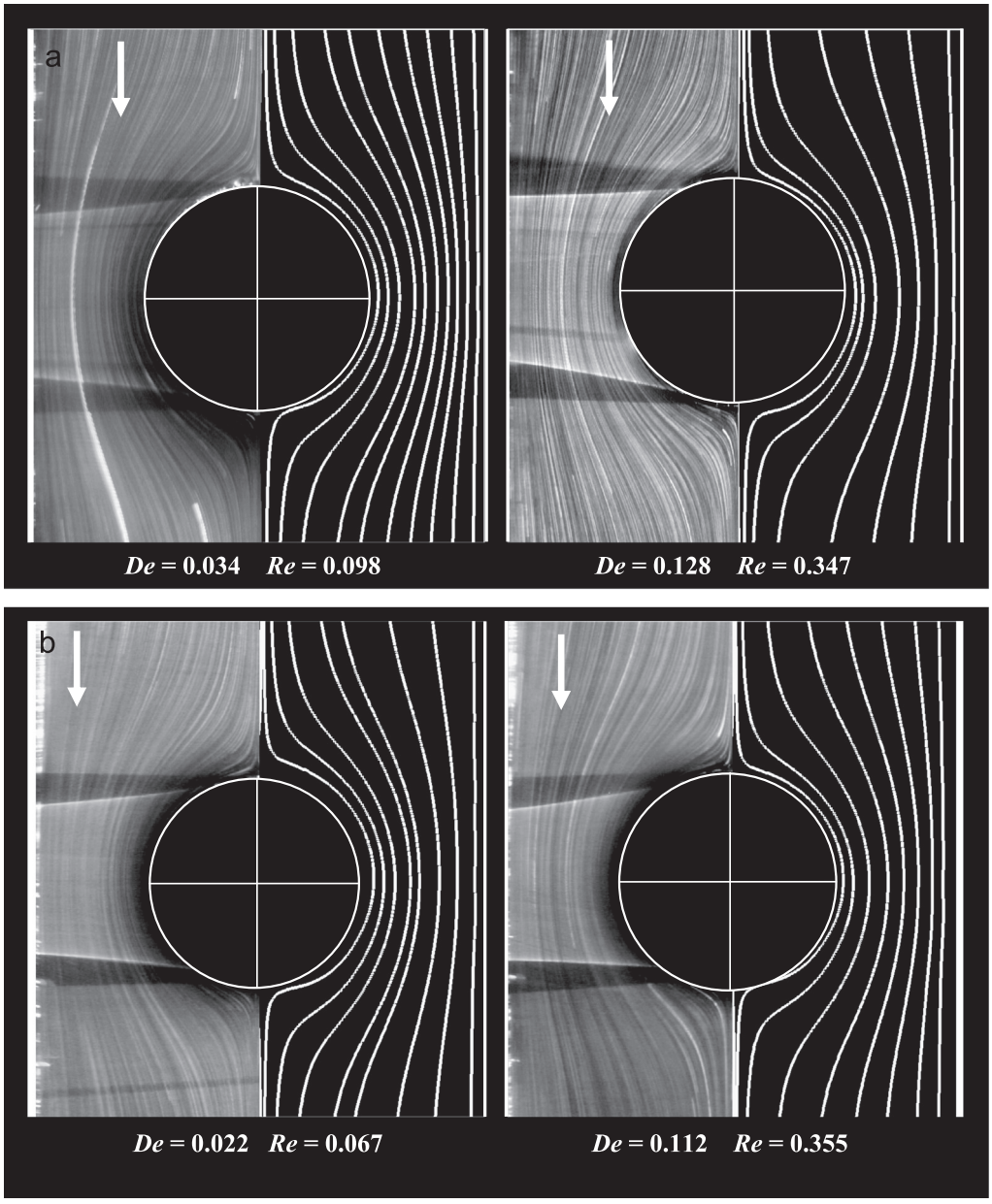

Fig. 18. Experimental (left) and numerical (right) flow patterns at the symmetry plane ($z/R=0$) for $AR=16$: (a) PAA200 fluid; (b) PAA400 fluid.

Comparing the Newtonian simulations (dashed line) with the viscoelastic simulations for $De=1.25$ at the same $Re=2.7$ (solid line) we conclude that the viscoelasticity leads to an increase in the required development length. For $AR=8$ and 2, Fig. 21b and c also shows an increase of the development length with De. We can also conclude from the various comparisons in Fig. 21 that at these conditions of low Re, the influence of inertia upon flow development length is significantly weaker than that of viscoelasticity. In addition, the observed increase of the development length with De agrees with the numerical study of Alves et al. (2001) for 2D cylinder flow of an Oldroyd-B fluid.

In the numerical investigation of Sahin (2013), the onset of 3D purely elastic instabilities occurs at De between 1.2 and 1.6. Since the viscosity ratio of the Oldroyd-B fluid used by Sahin (2013) ($\beta=0.59$) is lower than the viscosity ratio of the PAA200 Boger fluid used in this work ($\beta=0.82$), it is expected that the onset of instabilities in our simulations occurs at a higher critical De. However, even at $De=3.0$, shown in Fig. 21, we were unable to predict any instabilities in the flow. The modest resolution of the mesh used in this work, in comparison with the mesh used by Sahin (2013), can also artificially delay the onset of the flow transitions.

Figs. 22 and 23 show the spanwise evolution of the streamwise profiles of the streamwise velocity component at the $y/R=0$ centreplane for $AR=16$ and 2, respectively. Curves pertaining to different values of De are shown. Fig. 22 includes both experimental and numerical data and Fig. 23 includes only numerical data. For both AR cases, the fully developed velocity is higher on the centreline and decreases on approaching the end walls, as also happens for the Newtonian fluid flow (Ribeiro et al., 2012) and for the shear-thinning fluid flow as shown in Section 5.1. As expected, the fully developed velocity is the same upstream and downstream of the cylinder.

For the $AR=16$ geometry (Fig. 22), the velocity profiles are essentially similar for $z/R\leq 8$ and no velocity overshoots are

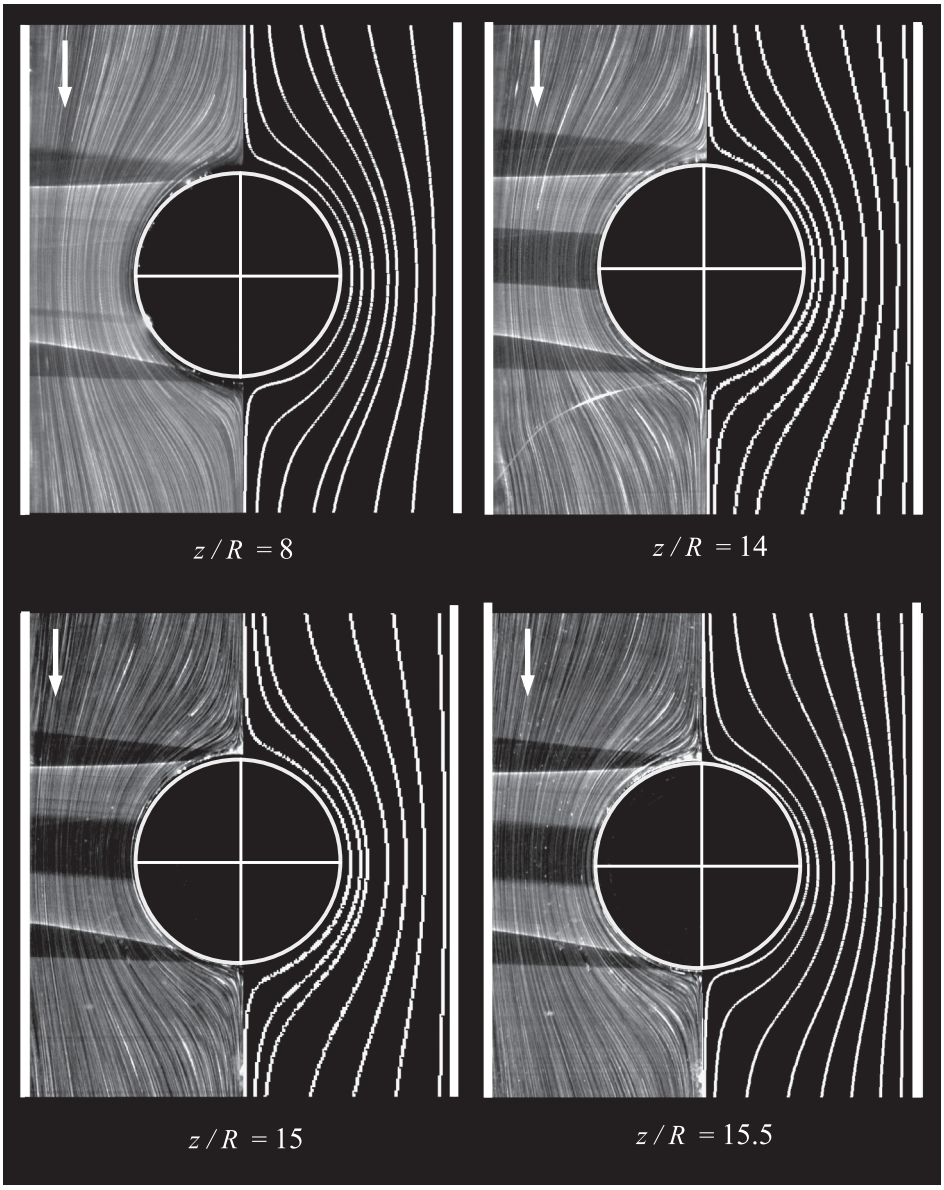

Fig. 19. Experimental (left) and numerical (right) flow patterns at different z-planes along the cylinder axis for $AR=16$, $De=0.13$ and $Re=0.35$ using the PAA200 Boger fluid.

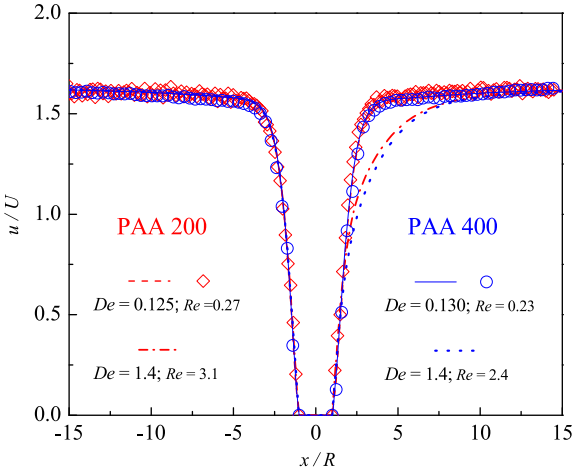

Fig. 20. Streamwise velocity profiles along the centreline ($y/R=0$, $z/R=0$) of the streamwise velocity component for the flow of Boger fluids PAA200 and PAA400 for $AR=16$. Comparison between experimental (symbols) and numerical predictions (lines).

observed. At the near end-wall planes ($z/R \geq 12$), the streamwise velocity profiles display a significant overshoot, localized at $x/R \approx -3$, followed by a reduction of the velocity, due to the approach of the cylinder, as was the case previously shown for the shear-thinning fluid. A fore–aft quasi-symmetric velocity profile is observed around the cylinder for the lower *De* flow case. The flow upstream of the cylinder is essentially independent of the *De* for all planes along the cylinder, in agreement with Fig. 21. However, downstream of the cylinder the location of the velocity peaks strongly depends on *De*, becoming less pronounced and occurring farther downstream from the cylinder as *De* increases, thus breaking the fore–aft symmetry. For the $De=0.09$ flow shown in Fig. 22, the numerical and the experimental data are in reasonable agreement.

In Fig. 23, corresponding to $AR=2$, a slight velocity overshoot is only observed in the planes closer to the end wall ($z/R=1.5$ and $z/R=1.8$) for the lower *De* downstream of the cylinder near $x/R \approx 3$. For all planes illustrated, the length required for the flow redevelopment downstream of the cylinder increases with *De*, as also observed for $AR=16$, and the velocity profiles are quasi-symmetric relative to $x/R=0$ for the lower *De*.

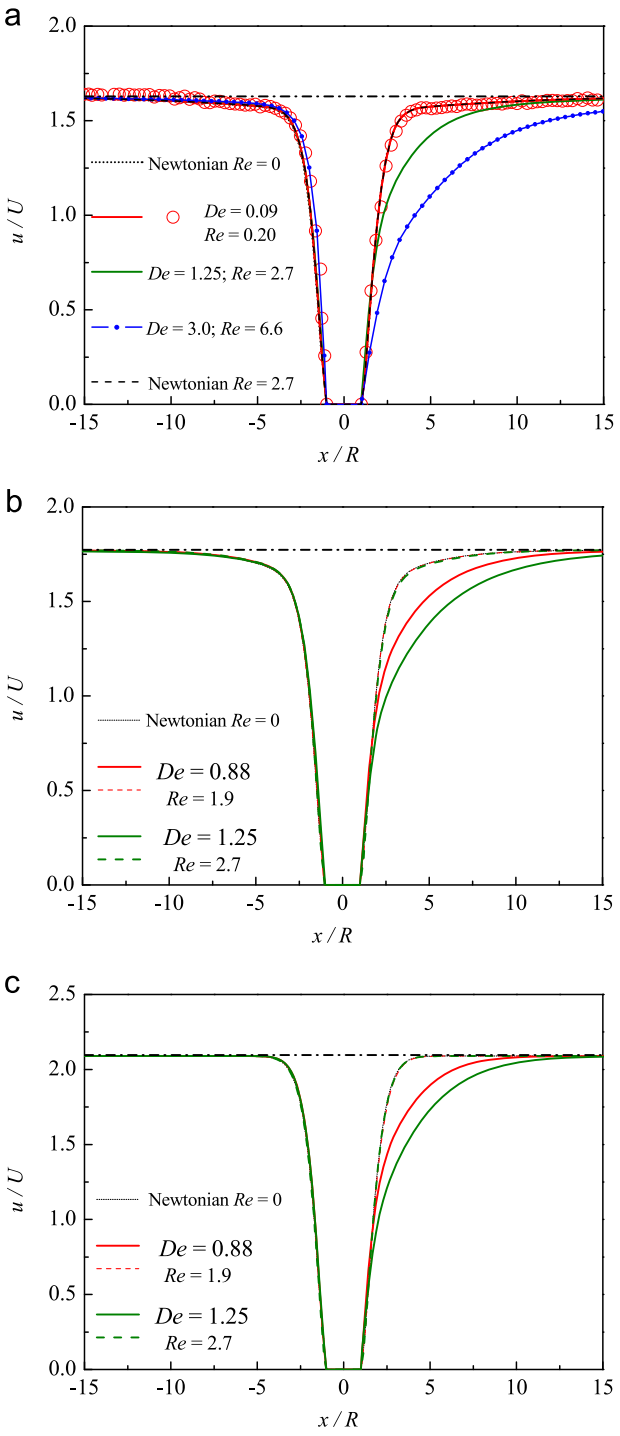

Fig. 21. Streamwise velocity component along the centreline ($y/R=0$, $z/R=0$) for the PAA200 Boger fluid flow as a function of *De*: (a) $AR=16$; (b) $AR=8$; (c) $AR=2$. Comparison between experimental (symbols), numerical predictions using the Oldroyd-B model (full lines) and numerical predictions for a Newtonian fluid at the same *Re* (dashed lines). The dash–dot lines are a guide to the eye and represent the fully developed velocity in the rectangular duct.

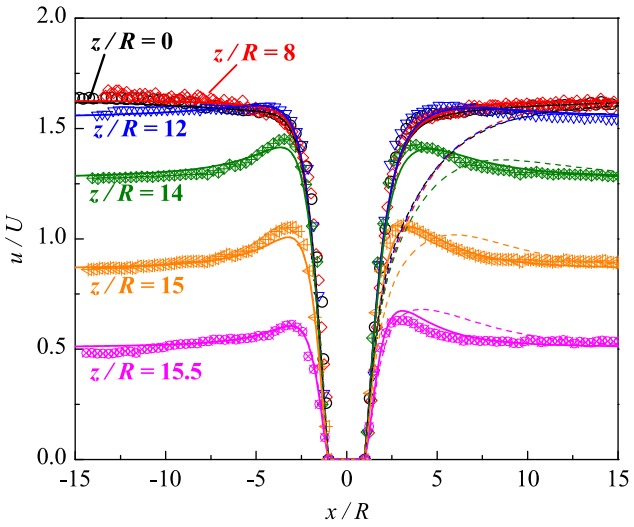

Fig. 22. Streamwise profiles of the normalized streamwise velocity taken at the $y=0$ centreplane at different values of the spanwise coordinate, z/R, for $AR=16$ and for PAA 200 Boger fluid: $De=0.09$, $Re=0.20$ – experimental (symbols) and numerical (full lines); $De=1.25$, $Re=2.7$ – numerical (dashed lines).

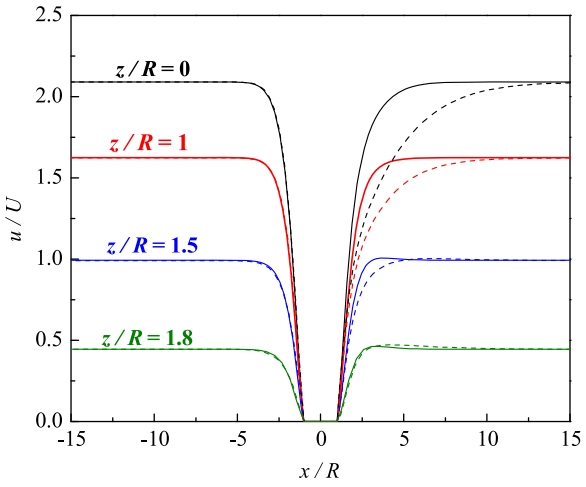

Fig. 23. Streamwise profiles of the normalized streamwise velocity taken at the $y=0$ centreplane at different values of the spanwise coordinate, z/R, for $AR=2$ and for PAA 200 Boger fluid: $De=0.5$, $Re=1.1$ (full lines) and $De=1.25$, $Re=2.7$ (dashed lines).

6. Conclusions

An experimental and numerical study was carried out on the flow past a confined cylinder placed in a rectangular duct with a 50% blockage ratio using a Newtonian, a shear-thinning and two Boger fluids. The flow was characterized experimentally using streak photography and PIV to quantify the complex flow field. The flow conditions investigated ranged from inertia-less and low *De* flow up to the onset of time-dependent flow, for aspect ratios $AR=16$, 8 and 2.

The measurements for the shear-thinning fluid show the appearance of an elastic instability upstream of the cylinder, at a critical Deborah number, De_c. For low *De*, the flow is symmetric relative to the planes $y=0$ and $z=0$ (the creeping flow of Newtonian fluids is also symmetric relative to the $x=0$ plane). When *De* exceeds a critical value, De_c, an elastic instability sets in and becomes more intense with the increase in *De*, and the flow becomes progressively asymmetric but remains steady until it eventually becomes time-dependent at higher *De*. At a constant *De*, the intensity of the asymmetry decreases when *AR* decreases, due to the increasing relevance of viscous effects in the vicinity of the end walls. The deceleration upstream of the cylinder and the subsequent velocity recovery downstream of the cylinder depend also on *AR* and *De*. As expected, the shear-thinning viscoelastic fluid shows a decrease of the fully developed non-dimensional velocity at the duct axis, compared with the corresponding fully developed velocity for the constant shear viscosity fluids (Newtonian and Boger fluids).

The results for the Boger fluids are particularly useful to isolate the elastic effects. Over the range of *De* studied for the Boger fluids, the flow patterns are symmetric and steady and the numerical predictions using the Oldroyd-B model fitted to their rheology matched very well with the experimental data. The velocity measurements with the Boger fluids show that for lower *De* elastic effects are negligible, but as *De* increases, the elasticity of the fluid leads to an increase of the required development length downstream of the cylinder, in agreement with the numerical simulations using the Oldroyd-B model. The velocity development length is also found to increase with an increase of *AR*.

For all fluids, the velocity peaks encountered near the end walls are enhanced by an increase in the Deborah number and are reduced as *AR* decreases as was previously seen for the Newtonian fluid (Ribeiro et al., 2012).

Acknowledgments

The authors acknowledge the financial support from FEDER, COMPETE and FCT (Portugal) through Project PTDC/EME-MFE/114322/2009 and scholarship SFRH/BD/44737/2008 (V.M. Ribeiro).

References

Adrian, R.J., 2005. Twenty years of particle image velocimetry. Exp. Fluids 39, 159–169.
Alves, M.A., Oliveira, P.J., Pinho, F.T., 2003. A convergent and universally bounded interpolation scheme for the treatment of advection. Int. J. Numer. Methods Fluids 41, 47–75.
Alves, M.A., Pinho, F.T., Oliveira, P.J., 2001. The flow of viscoelastic fluids past a cylinder: finite-volume high-resolution methods. J. Non-Newton. Fluid Mech. 97, 207–232.
Brown, R.A., McKinley, G.H., 1994. Report on the VIIIth international workshop on numerical methods in viscoelastic flows. J. Non-Newton. Fluid Mech. 52, 407–413.
Carreau, P.J., 1972. Rheological equations from molecular network theories. Trans. Soc. Rheol. 16, 99–127.
Dealy, J., Plazek, D., 2009. Time–temperature superposition. Rheol. Bull. 18, 16–31.
Entov, V.M., Hinch, E.J., 1997. Effect of a spectrum of relaxation times on the capillary thinning of a filament of elastic liquid. J. Non-Newton. Fluid Mech. 72, 31–53.
Fattal, R., Kupferman, R., 2004. Constitutive laws for the matrix-logarithm of the conformation tensor. J. Non-Newton. Fluid Mech. 123, 281–285.
Ferreira, H.H., 2006. Escoamento de fluidos Newtonianos e viscoelásticos em torno de um cilindro: estudo numérico de efeitos tridimensionais. Faculdade de Engenharia da Universidade do Porto (M.Sc. thesis. MSc on Fundamentals and Applications of Fluid Mechanics).
Kenney, S., Poper, K., Chapagain, G., Christopher, G.F., 2013. Large Deborah number flows around confined microfluidic cylinders. Rheol. Acta 52, 485–497.
Kumar, B., Mittal, S., 2006. Prediction of the critical Reynolds number for flow past a circular cylinder. Comput. Method Appl. Mech. Eng. 195, 6046–6058.
Li, F.C., Kinoshita, H., Li, X.B., Oishi, M., Fujii, T., Oshima, M., 2010. Creation of very-low-Reynolds-number chaotic fluid motions in microchannels using viscoelastic surfactant solution. Exp. Therm. Fluid Sci. 34, 20–27.
Li, X.B., Li, F.C., Cai, W.H., Zhang, H.N., Yang, J.C., 2012. Very-low-Re chaotic motions of viscoelastic fluid and its unique applications in microfluidic devices: a review. Exp. Therm. Fluid Sci. 39, 1–16.
Manero, O., Mena, B., 1981. On the slow flow of viscoelastic liquids past a circular cylinder. J. Non-Newton. Fluid Mech. 9, 379–387.
McKinley, G.H., 1991. Nonlinear Dynamics of Viscoelastic Flows in Complex Geometries (Ph.D. thesis). Department of Chemical Engineering, Massachusetts Institute of Technology, Cambridge.
McKinley, G.H., Armstrong, R.C., Brown, R.A., 1993. The wake instability in viscoelastic flow past confined circular cylinders. Philos. Trans. R. Soc. A 344, 265–304.
Nishimura, T., 1986. Flow across tube banks. In: Cheremisinoff, P. (Ed.), Encyclopedia of Fluid Mechanics. Gulf Publishing Company, Houston, pp. 763–785.
Oliveira, P.J., Pinho, F.T., Pinto, G.A., 1998. Numerical simulation of non-linear elastic flows with a general collocated finite-volume method. J. Non-Newton. Fluid Mech. 79, 1–43.
Phan-Thien, N., Dou, H.S., 1999. Viscoelastic flow past a cylinder: drag coefficient. Comput. Method Appl. Mech. Eng. 180, 243–266.
Poole, R.J., Alves, M.A., 2009. Velocity overshoots in gradual contraction flows. J. Non-Newton. Fluid Mech. 160, 47–54.
Poole, R.J., Escudier, M.P., Afonso, A., Pinho, F.T., 2007. Laminar flow of a viscoelastic shear-thinning liquid over a backward-facing step preceded by a gradual contraction. Phys. Fluids 19, 093101.
Ribeiro, V.M., Coelho, P.M., Pinho, F.T., Alves, M.A., 2012. Three-dimensional effects in laminar flow past a confined cylinder. Chem. Eng. Sci. 84, 155–169.
Richter, D., Iaccarino, G., Shaqfeh, E.S.G., 2010. Simulations of three-dimensional viscoelastic flows past a circular cylinder at moderate Reynolds numbers. J. Fluid Mech. 651, 415–442.
Sahin, M., 2011. A stable unstructured finite volume method for parallel large-scale viscoelastic fluid flow calculations. J. Non-Newton. Fluid Mech. 166, 779–791.
Sahin, M., 2013. Parallel large-scale numerical simulations of purely-elastic instabilities behind a confined circular cylinder in a rectangular channel. J. Non-Newton. Fluid Mech. 195, 46–56.
Sahin, M., Owens, R.G., 2004. A numerical investigation of wall effects up to high blockage ratios on two-dimensional flow past a confined circular cylinder. Phys. Fluids 16, 1305–1320.
Sahin, M., Wilson, H.J., 2007. A semi-staggered dilation-free finite volume method for the numerical solution of viscoelastic fluid flows on all-hexahedral elements. J. Non-Newton. Fluid Mech. 147, 79–91.
Sen, S., Mittal, S., Biswas, G., 2009. Steady separated flow past a circular cylinder at low Reynolds numbers. J. Fluid Mech. 620, 89–119.
Shiang, A.H., Lin, J.C., Öztekin, A., Rockwell, D., 1997. Viscoelastic flow around a confined circular cylinder: measurements using high-image-density particle image velocimetry. J. Non-Newton. Fluid Mech. 73, 29–49.
Shiang, A.H., Oztekin, A., Lin, J.C., Rockwell, D., 2000. Hydroelastic instabilities in viscoelastic flow past a cylinder confined in a channel. Exp. Fluids 28, 128–142.
Telionis, D.P., Gundappa, M., Diller, T.E., 1992. On the organization of flow and heat-transfer in the near wake of a circular cylinder in steady and pulsed flow. J. Fluid Eng.-Trans. ASME 114, 348–355.
Tenchev, R., Gough, T., Harlen, O.G., Jimack, P.K., Klein, D.H., Walkley, M.A., 2011. Three dimensional finite element analysis of the flow of polymer melts. J. Non-Newton. Fluid Mech. 166, 307–320.
Verhelst, J.M., Nieuwstadt, E.M., 2004. Visco-elastic flow past circular cylinders mounted in a channel: experimental measurements of velocity and drag. J. Non-Newton. Fluid Mech. 116, 301–328.
White, F.M., 1991. Viscous Fluid Flow, 2nd edition. McGraw-Hill, New York.
Williamson, C.H.K., 1996. Vortex dynamics in the cylinder wake. Annu. Rev. Fluid Mech. 28, 477–539.
Zdravkovich, M.M., 1997. Flow Around Circular Cylinders. Vol. 1: Fundamentals. Oxford University Press, New York.
Zdravkovich, M.M., 2003. Flow Around Circular Cylinders. Vol. 2: Applications. Oxford University Press, New York.